Research Square

Preprints are preliminary reports that have not undergone peer review.
They should not be considered conclusive, used to inform clinical practice,
or referenced by the media as validated information.

The AKAP1 ribonucleoprotein network integrates mitochondrial homeostasis, P-body dynamics and protein translation in cycling cells

Feliciello Antonio

feliciel@unina.it

University of Naples, Federico II https://orcid.org/0000-0002-7932-2170

Laura Rinaldi

University of Naples, Federico II

Emanuela Senatore

University of Naples, Federico II

Federica Moraca

University of Naples, Federico II

Chiara D'Ambrosio

National Research Council, Naples, Italy https://orcid.org/0000-0003-2810-9270

Francesca Rizzo

University of Salerno (I) https://orcid.org/0000-0003-1783-5015

Elena Alexandrova

University of Salerno

Rosario Avolio

https://orcid.org/0000-0001-9573-1110

Domenica Borzacchiello

University of Naples

Francesco Chiuso

Simona Aversano

University of Naples Federico II

Giovanni Sorvillo

University of Naples Federico II

Antonio Bianco

University of Naples, Federico II

Angela Flavia Serpico

University of Naples Federico II https://orcid.org/0000-0001-8649-5603

Daniela Eletto

University of salerno

Omar Torres-Quesada
Medical University of Innsbruck
Ludger Hengst
Medical University of Innsbruck https://orcid.org/0000-0002-0605-0223
Eduard Stefan
University of Innsbruck https://orcid.org/0000-0003-3650-4713
Paolo Maiuri
Università degli Studi di Napoli "Federico II"
Domenico Grieco
CEINGE Biotecnologie Avanzate, DMMBM University of Naples https://orcid.org/0000-0002-7131-5742
Andrea Scaloni
https://orcid.org/0000-0001-9362-8515
Bruno Catalanotti
University of Naples, Federico II

Article

Keywords:

Posted Date: February 25th, 2026

DOI: https://doi.org/10.21203/rs.3.rs-8873259/v1

License: This work is licensed under a Creative Commons Attribution 4.0 International License.
Read Full License

Additional Declarations: There is no duality of interest

Abstract

Integration of protein translation and mitochondrial activities represents a mechanism to rapidly adapt anabolic processes to specific cellular needs. This aspect is of particular importance for cell division when mitochondrial dynamics, oxidative phosphorylation and protein synthesis are timely coordinated to allow a faithful completion of cell cycle. However, the mechanisms coupling mitochondrial homeostasis to protein translation in cycling cells are largely unknown. Here, we report the identification of a molecular network assembled by AKAP1 at mitochondria that includes mRNA, components of the translation repression machinery (P-bodies) and mitotic kinases (CDK1/2). During the interphase, the AKAP1 complex dynamically coordinates cAMP signaling, mitochondrial activity, P-body dynamics and protein translation to ensure proper cell cycle progression. At mitosis, CDK-induced proteolysis of AKAP1 via a cullin-mediated ubiquitin pathway reduces oxidative metabolism, promotes mitochondrial fission and reshapes mRNA translation, finalizing the cell cycle. Disruption of this network impairs cell cycle progression.

These findings unveil a regulatory mechanism controlled by AKAP1 that functionally and dynamically links oxidative metabolism to protein synthesis in cycling cells. Targeting this biological node could help to restore deranged mitochondrial function in degenerative and proliferative disorders.

INTRODUCTION

Mitochondria are organelles fundamental for cellular energy supply and constitute intracellular sites where survival signals, cell respiration and metabolic pathways integrate and focus, adapting their activity, and shape in response to specific energetic needs[12]. Signaling events controlled by cAMP-dependent protein kinase (PKA) play an important role in different aspects of mitochondrial activity [3 4 5]. Localization of PKA at different intracellular compartments is mediated by A-Kinase Anchor Proteins (AKAPs), which direct and amplify the cAMP signaling to discrete target sites [6]. AKAP1, also known as D-AKAP1, is the prototypic mitochondrial AKAP that binds and targets PKA to the outer mitochondrial membrane (OMM)[7], controlling important aspects of mitochondrial metabolism and dynamics[8 9 10 11]. AKAP1 mRNA undergoes alternative splicing generating different AKAP1 variants, including AKAP149 (mouse ortholog AKAP121), AKAP100 and AKAP84[12]. The splice variants share a similar NH_2-terminal core segment that includes the mitochondrial targeting domain and the PKA binding motif, but diverge at the C-terminus [12]. AKAP1 also binds other signaling enzymes[13], phosphatases[14], cAMP-phosphodiesterase[15], transcription factors[16], hypoxia-induced ubiquitin ligase Siah2[13] and components of mTOR pathway[17], thus acting as a 'transduceosome' that integrates and transmits different molecular signals generated at distal sites to mitochondria. Interestingly, AKAP121/AKAP149 contains at its C-terminal core a Tudor domain of unknown function and a K-Homology domain (KH)[12 18]. This KH domain binds nuclear-transcribed mRNAs encoding for mitochondrial proteins, facilitating their translation and import into the organelle[19,20]. AKAP1 domain organization is highly conserved in Drosophila. In the fruit fly, AKAP1 binds components of the polysome translational machinery, including La-related protein 4

(LARP4) and Poly(A)-binding protein C (PABPC), and regulates the translation of AKAP1-associated mRNAs at mitochondrial sites, positively impacting on mitochondrial biogenesis and oocyte maturation[21]. A similar mechanism operates also in mammalian cells[22]. Interestingly, recent evidence unveiled an evolutionary conserved AKAP1-mediated hierarchical strategy that eukaryotic cells adopt to recruit and locally translate selected classes of short mRNAs encoding for components of the electron transport chain (ETC), exemplifying a sophisticated mechanism to efficiently deliver proteins to mitochondria[23,24].

Physical and functional communications between mitochondria and other cellular compartments contribute to regulate the rate of translation of mitochondrial proteins[25,26,27]. The temporary storage of mature mRNAs within non-membranous ribonucleoprotein (RNP) cytoplasmic condensates, namely processing bodies (P-bodies), represents an evolutionary conserved mechanism that finely controls the decay/translation repression of selected classed of mRNAs, dynamically reshaping the cellular proteome in response to stress conditions or specific metabolic needs[28 29 30]. Among the large number of proteins identified as resident of P-bodies, the deadenylating (CCR4-Not) and decay (Lsm1-7) protein complexes, decapping enzymes (DCP1/DCP2), activators of decapping enzymes (EDC3/EDC4 and PAT1), the mRNA helicase (DDX6) and ribonuclease (XRN1) are considered core components of these RNP condensates that control the translational repression and mRNA decay[31 32 33]. P-body dynamics is regulated by signaling pathways and stress signals and is crucial for cell cycle progression. In cycling cells, P-bodies assemble in G1, then increase in size in S/G2 phase and dissolve in mitosis, with no major changes in the number across the cell cycle[34]. Moreover, P-bodies RNA composition differentially changes during cell cycle, compared to cytoplasmic RNA content, indicating the existence of a sophisticated mechanism that controls cell cycle-dependent condensation/fate of selected classes of mRNAs. Despite the established role of P-bodies in critical aspects of RNA biology and protein translation, both under physiological or stress conditions, the link between cell cycle progression, P-body dynamics and protein translation and its impact on- and regulation by- the mitochondrial oxidative metabolism, are still poorly understood, as the molecular mechanisms involved.

Here, we report that, during early phases of cell cycle, the mitochondrial scaffold protein AKAP1 functions as a metabolic sensor that efficiently links oxidative metabolism to P-body dynamics and protein translation. Proteolysis of AKAP1 during the progression through G2/M phase promotes mitochondrial fission and P-body assembly, decreasing oxidative metabolism and protein synthesis. Genetic manipulation of the regulatory system controlled by AKAP1 profoundly affects the ability of cells to timely synchronize P-body assembly, protein translation and mitochondrial metabolism, and thus inhibits the faithful completion of the cell cycle.

RESULTS

Network analysis of the AKAP1-RNA interactome. AKAP1 is highly expressed in a broad variety of human cancers [35 36]. More specifically, AKAP1 is required for glioblastoma growth, both *in vivo* and *in vitro*[17].

Accordingly, we investigated the RNA interactome of AKAP1 in this tumoral context. To this aim, we performed native RNA immunoprecipitation followed by high-throughput sequencing in human glioblastoma cells (MG) transiently expressing V5-tagged wild-type (WT) AKAP1 (Fig. 1a). To dissect the contribution of specific domains to RNA binding, we also used two AKAP1 deletion mutants lacking the RNA-binding KH domain (Δ563–630)[20] or the Tudor domain (Δ709–786)[18] (Fig. 1b,1c **and Supplementary Figure S1a**). Cells transfected with an empty vector served as a negative control and the input RNA was sequenced to account for background transcript expression. RNA yield and quality assessments (**Supplementary Figures S1b and S1c**) demonstrated that deletion of the KH domain nearly abolished the RNA binding, as RIP-Seq from the Δ563–630 mutant yielded RNA quantities comparable to the negative control. This observation supports previous findings that the KH domain of AKAP1 is critical for RNA-binding activity[18 22]. In contrast, the Δ709–786 mutant retained detectable RNA-binding activity, with RNA yield approximately six-fold higher than background, despite the lower levels of the overexpressed protein compared to WT and Δ563–630 constructs, most likely due to the reduced translation or stability of mutant protein (Fig. 1c, **Supplementary Figure S1a**). Hierarchical clustering and principal component analysis (**Supplementary Figures S1d and S1e**) confirmed the high reproducibility among replicates and demonstrated that deletion of either domain significantly altered the AKAP1 RNA interactome. Full-length AKAP1 was associated with 909 transcripts ($Log_2FC > 2$, padj < 0.01), while the Δ563–630 and Δ709–786 mutants were associated with a markedly smaller number of RNAs (109 and 128, respectively). The three resulting transcript lists were intersected and the outcomes visualized as a Venn diagram (Fig. 1d). This analysis revealed that 784 transcripts were uniquely associated with WT AKAP1, 31 were specific to the Δ709–786 mutant, and 62 were unique to the Δ563–630 mutant.

To enhance specificity, we sought to refine the list of 784 transcripts uniquely associated with WT AKAP1 (Fig. 1d) by identifying only those showing preferential and specific enrichment in the WT condition. To this end, we applied an additional filtering step to exclude transcripts that were also enriched in one or both of the mutant conditions (Δ563–630 and Δ709–786). Importantly, to increase the sensitivity of this exclusion and account for potential technical variability in RIP efficiency, we used a less stringent cut-off ($Log_2FC > 1.5$, padj < 0.05) for identifying transcripts enriched in the mutants. All transcripts meeting this relaxed criterion in Δ563–630 or Δ709–786, or both, were removed. This approach resulted in a refined list of 544 transcripts selectively enriched in WT AKAP1 RIPs. To further increase confidence in RNA association, we filtered out low-abundance transcripts with read counts below 100, reducing the list to 374. Finally, to avoid the inclusion of transcripts that may have been secondarily enriched due to AKAP1 overexpression, we excluded genes that were differentially expressed in the input RNA from AKAP1-transfected versus empty vector–transfected cells ($|FC| > 1.5$, padj < 0.05). This multi-step refinement produced a final list of 359 high-confidence transcripts specifically bound to full-length AKAP1 (**Supplementary Table S1).**

Gene ontology (GO) enrichment analysis of the 359 high-confidence full-length AKAP1-associated transcripts revealed significant overrepresentation of genes involved in ribosome-related processes, mitochondrial electron transport and respiration (**Supplementary Figure S2a**). These components are

central to protein synthesis, oxidative phosphorylation and energy production - processes implicated in metabolic reprogramming and frequently affected in glioblastoma[37]. Pathway analysis highlighted functional enrichment in translation-associated processes, including aminoacyl-tRNA biosynthesis, ribosome biogenesis, and all major stages of translation (initiation, elongation, and termination; Figs. 1e and 1g). Additional enriched pathways include selenocysteine biosynthesis, signal recognition particle (SRP)-dependent co-translational targeting to membranes, and L13a-mediated translational silencing. These findings suggest that AKAP1 may regulate a wide range of key processes involved in redox balance and protein translation [38 39 40], all of which are implicated in glioblastoma progression[41 42 43 44]. CORUM protein complex enrichment analysis (**Supplementary Figure S2b**) revealed that AKAP1-bound transcripts encode components of mitochondrial oxidative phosphorylation machinery (e.g., cytochrome c oxidase and respirasome), cytoplasmic and mitochondrial ribosome, and the NOP56p-associated pre-rRNA processing complex. The latter is involved in snoRNA-guided modification of pre-rRNA and ribosome biogenesis, suggesting a potential role for AKAP1 in coordinating ribonucleoprotein assembly and ribosomal maturation.

To further understand the role of the Tudor domain in AKAP1's RNA-binding specificity and function, we examined RIP-Seq data obtained from the AKAP1 Δ709–786 variant. We focused on identifying Tudor domain–independent RNA targets by selecting 83 transcripts significantly enriched in both full-length and Δ709–786 AKAP1 RIPs ($Log_2FC > 2$, padj < 0.01), but not enriched in the Δ563–630 dataset (Fig. 1d). After excluding 23 transcripts also enriched in the Δ563–630 RIPs under relaxed thresholds ($Log_2FC > 1.5$, padj < 0.05), 17 with read counts below 100, and 2 differentially expressed upon full-length AKAP1 overexpression (Input AKAP1 vs Input Empty, |FC| > 1.5, padj < 0.05), we obtained a final list of 41 high-confidence transcripts (**Supplementary Figure S2c, Supplementary Table S23**), which were subsequently subjected to gene ontology, signaling pathway and CORUM network analyses. GO analysis revealed enrichment in transcripts encoding mitochondrial respiratory chain components and inner mitochondrial membrane proteins (**Supplementary Figure S2d**). These findings suggest that the Tudor domain is not required for AKAP1 binding to mitochondrial mRNAs. Consistently, pathway analysis confirmed that AKAP1 Δ709–786 preferentially binds mRNAs encoding for components of oxidative phosphorylation machinery (Fig. 1f), including COX8A, NDUFA4, SDHD, ATP6V0E1, and COX6A1 (Fig. 1h). CORUM complex analysis further highlighted enrichment in cytochrome c oxidase complexes (Fig. 1f), supporting a Tudor-independent mechanism for the regulation of both structural subunits and assembly factors of mitochondrial complex IV, a central component of aerobic respiration. To validate the RIP-Seq results, we performed RIP-qPCR on a selected panel of transcripts, including nine RNAs specifically associated with full-length AKAP1, five enriched in both WT and Δ709–786 RIPs, and three transcripts not enriched in any RIP condition. The qPCR results (Fig. 1i) were highly concordant with RNA-Seq findings, confirming the specificity and reproducibility of our RIP-Seq data.

In summary, AKAP1 association with RNA is highly dependent on the KH domain, whereas the Tudor domain contributes to target selectivity without being strictly essential for RNA binding. Full-length

AKAP1 predominantly associates with transcripts involved in mitochondrial respiration, ribosome biogenesis and protein translation.

Proteomic analysis of AKAP1 complexes by Proximity Ligation Assay (PLA). To dissect the protein-protein interaction (PPI) network assembled by AKAP1 in mammalian cells, we took advantage of the proximity labelling assay (PLA) strategy based on the use of Turbo ID, an engineered biotin ligase that uses ATP to covalently label proximal proteins with biotin[45]. Accordingly, we generated an AKAP1-V5-Turbo ID vector carrying the V5 epitope and the Turbo ID ligase fused to AKAP1. When expressed in HeLa cells, this vector allowed the generation of a recombinant construct able to biotinylate proteins within a range of 10–20 nm of proximity to AKAP1 (Fig. 2a). Cells transfected with a V5-Turbo ID vector were used for comparative purposes. In both cases, biotinylated proteins were loaded in parallel onto streptavidin-functionalized columns. Bound proteins were eluted separately and finally subjected to independent proteomic analyses. The dataset is available in the ProteomeXchange repository (http://www.proteomexchange.org/) under the identifier PXD070538. By comparing proteins identified through PLA in HeLa cells expressing AKAP1-V5-Turbo ID versus V5-Turbo ID (empty vector), we identified 65 protein entries, corresponding to 64 genes, which were specifically enriched in AKAP1-eluted fractions, compared to control samples (**Supplementary Figure S3a**). To validate proteomic data, we compared these putative AKAP1 interactors with currently known AKAP1-associated proteins from BioGRID[46], IntAct [47], MINT [48] and STRING databases. Among previously reported entries, a total of 15 proteins (23.4%) were detected in at least one of the above-reported databases, while 49 proteins (76.6%) appeared as novel AKAP1 interactors (**Supplementary Figure S3a**). A very negligible number of these proteins appeared in the CRAPome database, the repository of components detected in negative controls of affinity purification-mass spectrometry experiments [49], highlighting the validity of the experimental approach used (**Supplementary Figure S3b**).

To understand the most significant biological processes, molecular functions and cellular components associated with identified AKAP1-binding partners, we performed a dedicated functional enrichment analysis for gene ontology (GO) categories. GO analysis of AKAP1 interactors indicated that most enriched biological processes were related to the regulation of protein translation (Fig. 2b). On the other hand, GO enriched terms in the molecular function showed that AKAP1 partners were mainly related to mRNA binding (Fig. 2c). In parallel, a PPI network was calculated using the identified AKAP1-binding partners and the STRING database, showing that the former ones are strictly interconnected in a populated molecular assembly including 54 proteins (Fig. 2d). The network enriched (according to a dedicated clustering) in AKAP1 interactors involved in specific protein groups includes also a significant number of components of cytoplasmic stress granules (19 out of 64 interactors) or linked to Cdc20 phosphoAPC/C-mediated degradation of cyclin A (12 out of 64 interactors), and others (Fig. 2e).

AKAP1 interaction with components of the translation repression machinery. P-bodies are cytoplasmic granules composed of multiple ribonucleoproteins and mRNAs and are involved in the translation repression and RNA decay. Several AKAP1 interactors identified through PLA can be assigned to the protein cluster of “cytoplasmic granules”. Co-immunoprecipitation assays confirmed that AKAP1 forms a

stable complex with core components of P-bodies, including DDX6, Staufen and EDC3 (Fig. 3a-d). Moreover, AKAP1 coimmunoprecipitates with Ago2 and Dicer, two components of the RNA-induced silencing complex (RISC) that is fundamental for translation repression (Fig. 3a).

P-bodies are highly dynamic organelles, as the number and size of P-bodies can change in response to different stimuli [29], thus affecting protein translation and mRNAs turnover. Since AKAP1 interacts with components of P-bodies, we evaluated the impact of AKAP1 deletion on P-bodies dynamics. To this end, we generated an AKAP1 Knock-Out (AKAP1 KO) U87MG cell line and analyzed the effects of this genetic deletion on P-bodies assembly. As shown in Fig. 3e and 3f, the number of P-bodies in AKAP1 KO U87MG cells was significantly increased compared to WT cells. The effects of AKAP1 deletion on P-bodies number was reversed by re-expression of WT AKAP1 but not its ΔKH mutant, demonstrating that the RNA binding activity of AKAP1 is, indeed, required for P-body assembly (Fig. 3e and 3f). Next, we analyzed the impact of AKAP1 deletion on protein translation using a click-chemistry based approach (Fig. 3g-h). Briefly, cells were incubated with the amino acid analog L-homopropargylglycine (HPG)-alkyne and nascent protein synthesis was monitored through biotin-azide click reaction and western blot. The data of Fig. 3h indicate that AKAP1 is required for efficient protein translation, since AKAP1 KO cells displayed a significant lower rate of newly translated proteins, compared to control cells. The ability of AKAP1 to bind mRNAs is also important for the cell oxydative metabolism, since the overexpression of the ΔKH mutant results in a decreased Oxygen Consumption Rate (OCR) compared to cells overexpressing the WT protein (Fig. 3i). This decrease results in a lower ATP production rate and a lower spare respiratory capacity (Fig. 3j).

AKAP1 targets mitotic kinase CDK1 to mitochondria. The PLA data set of the identified AKAP1 interactors includes the cyclin-dependent kinase 1 (CDK1), an important regulator of cell cycle progression[50 51]. Co-immmunoprecipitation assays using lysates from growing cells did not show any significant binding between AKAP1 and CDK1 (**Suppl. Fig. S4**). Since the expression and activity of CDK1 are strictly regulated throughout the cell cycle, we analyzed the AKAP1/CDK1 interaction in distinct phases of cell cycle. In particular, HeLa cells were synchronized at G1/S boundary by double thymidine block and then released into the cell cycle by thymidine washing (Fig. 4a). Interestingly, co-immunoprecipitation assays revealed a strong binding between CDK1 and AKAP1 in thymidine-arrested cells, which was almost lost in thymidine-released cells (Fig. 4b). Moreover, deletion mutagenesis and co-immunoprecipitation assays demonstrated that the C-terminal region of AKAP1 was, indeed, required for a stable interaction with CDK1 (Fig. 4b).

Next, we evaluated the intracellular distribution of AKAP1 and CDK1 in cells synchronized at G1/S boundary or in cycling cells by in-situ immunostaining analysis. As shown in Fig. 4c and Fig. 4d, in synchronized cells, a significant fraction of CDK1 colocalized with the mitotraker signal, a specific marker of mitochondrial compartment. In contrast, cells released from thymidine block showed a predominant nuclear staining for CDK1. Interestingly, mitochondrial localization of CDK1 in growth-arrested cells required AKAP1. Thus, genetic downregulation of AKAP1 delocalized CDK1 staining mostly in the nuclear compartment (Fig. 4c and 4d). Similarly, downregulation of endogenous AKAP1 in

synchronized HeLa cells also decreased the amount of CDK1 that co-purified with mitochondrial proteins (Fig. 4e-f). Moreover, phosphorylation of mitochondrial CDK1 substrates was markedly downregulated by AKAP1 knock-down (Fig. 4e-g).

AKAP1 is a direct target of CDK kinases and CDK1 phosphorylation affects AKAP1/PKA complex formation. The data above indicate that AKAP1 and CDK1 form a dynamic complex in cycling cells and suggested that AKAP1 can be also a target of CDK1. Phosphorylation of cellular substrates by mitotic kinases often results in a slower migration rate of phosphorylated proteins. Accordingly, we analyzed the migration rate of AKAP1 in SDS-PAGE gel using total lysates from synchronized HeLa cells at G1/S boundary or following the release from thymidine block. As shown in Fig. 4h and 4i, the thymidine release retarded the migration rate of AKAP1 protein compared to control baseline. This effect was reversed by treating cells with a specific CDK1 inhibitor, suggesting that AKAP1 is, indeed, a CDK1 target in cycling cells.

CDK1 and CDK2 share a highly overlapping substrate specificity and are known to phosphorylate both canonical S/T-P-X-K/R consensus motifs and non-canonical sites during cell cycle progression[52]. Sequence analysis of AKAP1 did not reveal conserved canonical CDK1/2 consensus motifs. However, interrogation of publicly available phosphoproteomic databases identified five conserved phosphorylation sites (S55, S220, S315, T322, and S449) in both human and murine AKAP1[53 54 55]. To determine whether AKAP1 is a direct substrate of CDK kinases, we performed in vitro phosphorylation assays using recombinant CDK2/Cyclin A complex. These experiments demonstrated that AKAP1 is efficiently phosphorylated in vitro, confirming that AKAP1 is a direct CDK1/2 substrate (Fig. 4j). Mutation of all five identified sites to alanine markedly reduced CDK2-dependent phosphorylation compared to wild-type AKAP1 and to partial mutants (Fig. 4k and 4l), suggesting that CDK1/2 phosphorylates AKAP1 at multiple sites and exhibits broad site tolerance. Together, these data indicate that AKAP1 is directly phosphorylated by CDK kinases, with CDK1 mediating AKAP1 phosphorylation in cycling cells, while CDK2 demonstrates intrinsic substrate competence in vitro.

Serine-315 and threonine-322 are located within the PKA binding domain (RBD) of AKAP1 (Fig. 4m). This domain is structured in an amphipathic α-helical wheel that is required for optimal binding to the regulatory subunit of PKA holoenzyme. To understand if phosphorylation of these sites interferes with the interaction between AKAP1 and PKA-RIIβ subunit (RIIβ), we generated two phospho-mimetic mutants carrying a single (S315D) or double (S315D/T322D) S/T-to D substitution and tested their ability to bind to RIIβ. Co-immunoprecipitation assays demonstrated that S315D mutant expressed in HeLa cells lost its ability to interact with RIIβ, compared to wild-type protein (Fig. 5a). Furthermore, *in vitro* GST pull-down experiments showed that the binding between S315D/T322D mutant and RIIβ was dramatically decreased, compared to wild type protein or an AKAP1 mutant carrying double S315/T322-to A substitutions (S315A/T322A) (Fig. 5b and 5c).

Phosphorylation of AKAP1 affects the stability α-helical wheel conformation. To elucidate the molecular basis of AKAP1 bond loss after phosphorylation, we constructed the homology model of the AKAP1

amphipathic α-helix complexed to the dimerization domain (D/D) of RIIβ (AKAP1/RIIβ$_{D/D}$) (Fig. 5d and **Supplementary Fig. S5a-b**). One μs of conventional Molecular Dynamics simulations (cMDs) demonstrated the stability of the model (**Supplementary Fig. S6a-b**). To clarify the role of S^{315} and T^{322} in RIIβ$_{D/D}$ binding, the cMD predicted binding mode was further refined by means of a well-tempered funnel metadynamics simulation (FM) (Fig. 5e). This methodology simulated the binding-unbinding events of the WT-AKAP1 amphipathic α-helix and allowed us to extract the most energetically stable binding conformations. As shown in Fig. 5f, the free energy surface (FES) retrieved two isoenergetic minima (I and II) in which the amphipathic α-helix of WT-AKAP1 was oriented in opposite directions, exhibiting an approximate 180° rotation between them. Both binding modes showed that the main interactions were mediated essentially by hydrophobic patterns between I^{306}, A^{310}, L^{313}, I^{314}, V^{317}, I^{318}, A^{321} and F^{325} of WT-AKAP1 and L^{13}-L^{21} of the symmetrical interface of RIIβ$_{D/D}$; interestingly, S^{315} and T^{322} were not directly involved in the binding but remained solvent-exposed. Notably, the degeneracy of these two isoenergetic states and their nearly identical interaction patterns were fully consistent with the dimeric and highly symmetric nature of the RIIβ D/D domain being engaged. To further confirm this hydrophobic pattern, the FES was reweighted as function of the amphipathic α-helix contact map with RIIβ$_{D/D}$ (**Supplementary Fig. S7 a-b**), retrieving two energetic minima (III and IV). Basin III corresponded to the deepest energetic minimum and showed good overlap with the binding mode derived from the 1 μs cMD, demonstrating that the cMD efficiently detected the pattern of hydrophobic interactions (**Supplementary Fig. S7 a-b**). To evaluate the S^{315}/T^{322} di-phosphorylation effect on the AKAP1 amphipathic α-helix in its unbound state, we performed three independent cMDs of 500 ns each and compared the secondary structure map of this di-phosphorylated system (Fig. 5h) with that of the WT-AKAP1 and S315D/T322D (D2ST-AKAP1) counterparts (Fig. 5g and 5i, respectively). Results clearly showed that phosphorylation promoted α-helix destabilization by inducing a β-turn conformation more pronounced around the phosphorylated S315 and T322 positions (Fig. 5h). The D2ST-AKAP1 mutation exhibited an even stronger structural destabilization with extended coil and β-turn conformations becoming dominant (Fig. 5i). A partial destabilization of the di-phosphorylated AKAP1 amphipathic helix was observed also when it is bound to RIIβ$_{D/D}$ (Fig. 5j-k and **Supplementary Fig. S8c, f**), while the helicity was maintained both in the WT-AKAP1 (Fig. 5j-k and **Supplementary Fig. S8a, d**) and the double S31A/T322A mutation (A2-AKAP1) (Fig. 5j-k and **Supplementary Fig. S8b, e**) as demonstrated by Root Mean Square Deviation (RMSD) and Fluctuations (RMSF) analysis (**Supplementary Fig. S8g-h**, respectively), in agreement with the above-reported experimental evidences. Taken together, the computational studies suggested that phosphorylation of AKAP1 amphipathic α-helix by CDK1 led to a loss of affinity for the RIIβ$_{D/D}$ domain, by affecting the stability of the helical conformation required to engage its hydrophobic binding interface.

Impact of AKAP1 phosphorylation on mitochondrial activity in cycling cells. AKAP1 is the main mitochondrial scaffold for PKA, whose localization on the outer mitochondrial membrane is critical for mitochondrial dynamics (fusion and fission) and metabolism[56 57 58]. The inability of S315D/T322D AKAP1 mutant to bind RIIβ impaired the physiological mitochondrial dynamics. In fact, HeLa cells expressing the S315D/T322D mutant displayed more rounded mitochondria, whose shape indicated an

increased fission, compared to controls (Fig. 6a, b). The effects of the impaired binding between the S315D/T322D and RIIβ was also reflected by the observed decrease of the oxygen consumption rate (OCR) in HeLa cells expressing the mutant protein, compared to cells with WT protein (Fig. 6c, d). Decreased OCR displayed by S315D/T322D expressing cells results in a mild decrease of oxidative ATP production, with no major changes in the glycolytic ATP production (Fig. 6e). Conversely, the overexpression of the S315A/T322A mutant did not alter mitochondrial morphology (Fig. 6a, b), causing instead an increase of both OCR and mitochondrial ATP production (Fig. 6c, 6d and 6e). These data confirmed that phosphorylation of AKAP1 at the PKA binding domain impacts the mitochondrial morphology and activity.

PKA activity is fundamental to dynamically integrate metabolic pathways and cell cycle[59 60]. Recent evidence indicates that cAMP signalling acts as an upstream regulator of cell cycle progression in mammalian cells[61]. Accordingly, we found that HeLa cells expressing S315A/T322A mutant were mostly arrested or delayed at G0/G1 phase of the cell cycle, compared to controls (cells transfected with empty vector or with WT AKAP1) (Fig. 6f), suggesting that alterations of mitochondrial metabolism induced by the mutant protein are sensed by the cell cycle machinery as an inhibitory constraint. We then measured the OCR in HeLa cells transfected with the empty vector or expressing the WT AKAP1 and S315A/T322A mutant. The assay was performed under basal conditions or in the presence of oligomycin (an ATP synthase inhibitor), carbonyl cyanide-4-(trifluoromethoxy) phenylhydrazone (FCCP) (a mitochondrial protonophore uncoupler), and rotenone plus antimycin A (two mitochondrial transport chain inhibitors). Pharmacological treatment with inhibitors was used to discriminate the basal versus the ATP-linked OCR. The OCR of HeLa with empty vector or with the WT AKAP1 was dramatically decreased after the release from thymidine block, while no significant effects were evident in cells expressing S315A/T322A mutant (Fig. 6g and 6h).

Proteolysis of AKAP1 at mitosis reshapes mitochondrial morphology and activity. The data above indicate that AKAP1 is phosphorylated by the mitotic kinases CDK1/2 with a major impact on mitochondrial morphology and activity. Fluctuations of protein levels during cell cycle progression controlled by mitotic kinases synchronize key cellular activities to ensure the correct timing and progression throughout different phases of cell cycle[62 63]. Accordingly, we tested if AKAP1 stability was regulated by the cell cycle machinery. To this end, HeLa cells were synchronized by double thymidine (TIM) block and then released in the cell cycle. We monitored the levels of cyclin B as a marker of onset of mitotic phase[64]. As shown in Fig. 7a and 7b, cells exiting the G1/S boundary and approaching G2/M-phase showed a significant increase of AKAP1 levels. At the onset of M-phase, we observed a marked downregulation of AKAP1 levels (Fig. 7a and 7b) that was reversed by treating the cells with a specific CDK1 inhibitor (Ro3306) (Fig. 7c and 7d). The progression through the cell cycle is tightly regulated by the activity of the ubiquitin-proteasome system (UPS) that controls the stability of a variety of cell cycle-regulated proteins[65 66]. In this context, Cullin-RING ubiquitin ligases (CRL) constitute a large family of ubiquitin ligases that, in response to mitotic kinases, ubiquitinate and target cell cycle regulated proteins, including CDK inhibitors and activators, to proteasome [67]. We found that pre-treatment of HeLa cells

with a specific CRL inhibitor, MLN4924, reversed mitotic proteolysis of AKAP1 (Fig. 7e, 7f and 7g), indicating that the stability of AKAP1 is controlled by a CRL-UPS axis during cell cycle progression. Next, we tested if phosphorylation of AKAP1 at CDK1/2 sites was required for its proteolysis. Figure 7h and 7i show that phospho-mutant AKAP1-5Ala was quite stable during cell cycle progression and was not degraded by the cell cycle machinery. Interestingly, as shown in Fig. 7h and 7j, expression of the AKAP1-5Ala mutant affected the fluctuations of cyclin B levels, most likely due to impairment of cyclin B degradation after mitotic exit, with no major effects on cyclin E levels, a key regulator of G1/S-phases of the cell-cycle. This finding suggests that phosphorylation and degradation of AKAP1 are necessary events for the correct progression of cells through M-phase of cell cycle.

Mitochondrial dynamics is necessary for proper intracellular distribution of the organelles and to ensure the correct mitochondrial functioning in response to specific metabolic needs. Mitochondria change their shape and size during cell cycle progression, undergoing to fission during S and M phases, while forming a large network in G1 and G2 phases. The different morphological and functional state of mitochondria in cycling cells subserves as a mechanism to provide the correct amount of ATP and metabolic intermediates that cells require during distinct phase of cell cycle [68 69]. We confirmed the modification of the mitochondrial shape in course of cell cycle progression by monitoring mitochondrial dynamics in synchronized, cycling HeLa cells. Figure 7k shows that cells at G1/S boundary display mitochondria mostly with a rounded shape. The release of cells from thymidine block induced a time-dependent accumulation of mitochondria with a more tubular, interconnected morphological phenotype (Fig. 7k). At onset of mitotic phase, mitochondria reshape and acquire a more rounded morphological aspect typical of mitochondrial fission (Fig. 7k). Mitochondrial morphology often reflects the metabolic state of the cell. Based on this observation, we monitored the metabolic profile of synchronized HeLa cells by measuring the OCR and ECAR. Thymidine-blocked HeLa cells showed a higher OCR, characterized by an increased basal respiration and higher ATP production rate, compared to cycling cells (Fig. 7l). These findings indicate that changes in the mitochondrial morphology occurring during cell cycle progression are linked to a cellular metabolic reprogramming in response to specific energetic needs.

AKAP1 controls P-body dynamics and translation in cycling cells. Recent evidence indicates that nucleation of ribonuleoprotein condensates, as P-bodies, is finely regulated through cell cycle, these condensates increase in their size and number during transition from G1 to G2-phase, while dissolving when cells approach M-phase[70]. Given the role of AKAP1 in P-bodies assembly, we analyzed the impact of AKAP1 deletion in P-body dynamics in synchronized, cycling cells by monitoring the staining of DDX6, the core component of P-bodies. As shown in Fig. 8a and 8b, in control cells, the transition from G1/S-boundary to G2/M-phase was accompanied by a significant increase in the number of P-bodies, compared to baseline. Conversely, genetic knock-down of AKAP1 increased the number of P-bodies in thymidine-arrested cells, while no major effects were evident in cells re-entering the cell cycle (Fig. 8a and 8b). Since phosphorylation of AKAP1 is necessary for its degradation, we evaluated if/whether phosphorylation was also necessary to regulate P-body dynamics. Figure 8c and 8d show that re-

expression of wild type AKAP1 in AKAP1-KO U87MG cells, but not its phosphorylation-defective mutant (AKAP1-5Ala), restored the number of P-bodies to control values.

Considering the variation of P-bodies number during cell cycle progression and their increase in AKAP1-depleted cells, we wondered if also the global translation of the cell was also affected. A click-chemistry based approach revealed a global increase of protein translation during the cell cycle progression, which was partially reversed by the treatment with the CDK1 specific inhibitor Ro3306 (Fig. 8e). The increase of translation rate exhibited by control cells during cell cycle progression was not reversed by AKAP1 silencing. Notably AKAP1-silenced cells, when released from thymidine block, exhibited a differential pattern of translated proteins (Fig. 8f), suggesting that AKAP1 contributes to qualitatively regulating the translation of selected classes of mRNAs, rather than impacting on global protein synthesis.

DISCUSSION

Here, we report a mechanism that functionally links mitochondrial shape and metabolism to protein synthesis in cycling cells. We found that mitochondrial AKAP1 works as a metabolic sensor that binds mRNA and proteins of the translation repression machinery and finely regulates protein translation in a cell cycle-dependent manner. Cullin-mediated proteolysis of AKAP1 at mitosis induced by CDK1/2 attenuates oxidative metabolism and promotes mitochondrial fission, two essential steps for the safeguard mitosis completion. Genetic manipulation of this regulatory system markedly affected mitochondrial activity and protein translation, and induced cell cycle arrest.

Protein translation is controlled at multiple levels and requires the coordinated action of several regulatory mechanisms[71]. Condensation of ribonucleoprotein complexes within cytoplasmic aggregates, namely P-bodies, is an essential mechanism to temporarily store or degrade untranslated mRNAs. By dynamically regulating the turnover/translation of mRNAs, P-bodies finely shape the cellular proteome, playing a critical role under physiological and stress conditions [28 72]. Control of protein translation is of particular importance in growing cells as it sets the timely passage through distinct phases of cell cycle, in which the synthesis of specific classes of proteins are finely regulated. Dynamic recruitment of selected ribonucleoprotein complexes within P-bodies is controlled during the progression through the cell cycle, as P-bodies condensate at G1 phase, enlarge at interphase, and dissolve during mitosis[70]. However, the mechanism(s) controlling cell cycle-dependent P-body assembly/disassembly and its link to metabolic pathways have not been yet characterized.

AKAP1 acts as a PKA-scaffold protein that regulates cAMP cascade directed to mitochondria, functionally coupling signaling events generated by hormones at cell membrane to mitochondrial metabolic needs[73]. AKAP1 also binds nuclear-encoded mRNAs for mitochondrial proteins, playing an important role in translation and import of mitochondrial proteins within the organelles[20]. Original work demonstrated a role of KH domain of AKAP1 in mediating the translation of mRNAs encoding for mitochondrial proteins involved in steroid biosynthesis and SOD-mediated anti-oxidant responses [20 8]. Recent evidences suggested that AKAP1, indeed, recruits a large set of mRNAs encoding for short

proteins involved in oxidative phosphorylation, thus substantially contributing to mitochondrial activity [22]. Here, we extend these observations and found that AKAP1 assembles a ribonucleoprotein complex that includes essential elements of the translational machinery and core components of P-bodies. By interacting with RNA and RNA-binding proteins, AKAP1 dynamically controls P-body dynamics. Thus, genetic downregulation of AKAP1 significantly increased the number of P-bodies and markedly inhibited protein translation. The KH domain of AKAP1 is, indeed, required for AKAP1 effects on P-bodies. These findings support a model whereby AKAP1 should employ its own RNA-binding activity to regulate the shuttling of selected classes of transcripts between P-bodies and mitochondria, thus regulating the rate of translation of mitochondrial proteins. This mechanism would accommodate protein synthesis in response to changed mitochondrial metabolic requirements under specific cellular needs. In this context, protein translation is tightly regulated through cell cycle, increasing during interphase to support cell growth and function, and pausing during mitosis transition where most of cellular energetic stores are used for cell division[74]. Phosphorylation of translation initiation factors by cell cycle-dependent protein kinases is an important regulatory mechanism to control translation initiation[75]. Our findings add an additional layer of complexity to the mechanisms underlying cellular proteostasis and show that AKAP1, by modulating P-body dynamics, seems to control the rate and the timing of protein translation during cell cycle progression. The role of AKAP1 in protein synthesis in cycling cells is functionally linked to its ability to regulate oxidative metabolism. Interestingly, we found that during the early late phases of cell cycle, the resumption of protein synthesis is accompanied by a time-dependent accumulation of mitochondria with a more tubular, interconnected morphological phenotype, and a decrease of the oxygen consumption rate, indicating a dynamic regulation of mitochondrial activity in response to specific cell cycle needs.

Evidence indicates that a fraction of cyclin B1/CDK1 protein complex can be localized within the mitochondrial matrix, where it phosphorylates proteins of the respiratory chain and positively impacts on bioenergetic reactions and energy production required for cell division [76]. The regulation of mitochondrial activities by CDK1 is an expanding research field and involved mechanisms underlying mitochondrial fusion/fission machinery, SOD-mediated antioxidant response, cell survival, metabolic rewiring in drug-resistant cancer cells and others pathways [77 78 79]. Despite the established role of CDK1 in mitochondrial activities, the mechanism(s) underlying CDK1 translocation to the mitochondrial compartment is still largely unknown. We report that AKAP1 forms a complex with CDK1 in cell cycle-dependent manner. The interaction with the C-terminal segment of AKAP1 regulates the targeting of CDK1 to mitochondrial compartment. Here, CDK phosphorylates a variety of yet identified protein substrates, and modifies also AKAP1 at multiple sites. Two of these phosphorylation sites are located within the amphipatic helical wheel of AKAP1 required for its binding to PKA. Molecular dynamics studies and *in vitro* binding assays demonstrated that phosphorylation of both residues markedly impaired the binding affinity of PKA to AKAP1. Indeed, funnel metadynamics, reweighted free-energy surfaces and long-timescale cMD simulations identified two degenerate and energetically stable binding modes in which the AKAP1 amphipathic α-helix engaged the RIIβ D/D domain through a well-defined hydrophobic pattern. Phosphorylation of serine-315 and threonine-322, however, markedly destabilized

the helical conformation required for this interface, promoting β-turn formation and reduced helicity in both bound and unbound states. This structural rearrangement explained the impaired engagement of the D/D domain observed experimentally in phospho-mimetic mutants. Thus, in cell-based systems, expression of phospho-mimetic AKAP1 mutants within the PKA binding domain severely affected oxidative phosphorylation and promoted mitochondrial fission. These findings indicate that the activation of mitotic kinases, by preventing PKA binding to AKAP1, rapidly attenuates oxidative phosphorylation. Our findings are consistent with a previous observation linking CDK1 activation to the dynamic anchoring of RIIα-PKA holoenzyme to mitochondrial AKAP1 during the meiotic cycle of oocytes. By modulating the AKAP1•PKA interaction, CDK1 controls the temporal and spatial activation of PKA on mitochondria, playing a fundamental role for oocyte maturation [80].

During mitosis, CDKs-mediated phosphorylation of AKAP1 is eventually coupled to its proteolysis by a cullin-mediated proteasomal pathway. Downregulation of AKAP1 paralleled P-bodies assembly and translation/repression of selected classes of mRNAs, downregulation of oxidative phosphorylation and induction of mitochondrial fission. The latter event is an important prerequisite for proper redistribution of duplicated mitochondria to daughter cells. These findings support a model whereby mitotic kinases, by regulating the function and stability of AKAP1, should finely integrate protein synthesis and mitochondrial activity in cell cycle-dependent manner. Of interest is the finding that AKAP2, an actin-associated PKA anchor protein that coordinates cell migration and motility, is degraded during mitosis transition by a polo-like kinase (PLK1)-beta transducin repeat-containing protein (βTrCP)-dependent pathway [81]. Preventing AKAP2 proteolysis resulted in actin defects and aberrant mitotic spindles formation, pointing to a role of AKAP2 in coordinating cytoskeletal events underlying mitosis completion. The identification of AKAP1 and AKAP2 as targets of mitotic kinases indicates the existence of a more general mechanism mediated by the ubiquitin-proteasomal system to locally regulate the stability and activity of AKAP-anchored signaling complexes in cycling cells[81]. Further investigations will clarify the role of the mitotic E3-biquitin ligase in controlling the stability of AKAP1 and will define its role in the regulation of molecular events underlying mitochondrial dynamics and activity during cell cycle progression.

The essential role of AKAP1 in critical aspects of cell physiology is of particular importance for understanding the pathogenic role of derangement of AKAP1-controlled activities in human degenerative and proliferative disorders. Downregulation of AKAP1 has been causally linked to cardiovascular and neurodegenerative diseases, whereas upregulation of AKAP1 levels is mechanistically linked to proliferative disorders, including cancer[82 83 17]. In GBM cells, we discovered that AKAP1 promotes a metabolic rewiring that switches the oxidative metabolism to a more glycolytic pathway, a mechanism known as ‘Warburg effect’. Accordingly, we found that AKAP1 regulates the cellular proteome in GBM cells, thus contributing to anabolic pathways required for rapid cell growth.

Altogether, the results reported in this study unveil an important regulatory mechanism operated by mitochondrial AKAP1 that functionally links oxidative metabolism to protein synthesis in cycling cells (Fig. 8g). Understanding the level of complexity of AKAP1-assembled ribonucleoprotein complexes at

mitochondrial compartment and defining the hierarchy of signaling events regulating this important biological node in cycling cells will likely contribute to the development of novel therapeutics for the treatment of degenerative and proliferative disorders.

MATERIALS AND METHODS

Cell Culture and synchronization procedures. The human glioblastoma cell line U87MG was cultured in Dulbecco's Modified Eagle Medium (DMEM) (Euroclone, Milan, Italy) supplemented with 10% fetal bovine serum (HyClone™, Cytiva, Marlborough, MA, USA), 2 mM L-glutamine, 100 U/ml penicillin, 100 µg/ml streptomycin (all from Euroclone), and 250 ng/ml amphotericin B (Sigma-Aldrich, Burlington, MA, USA). HeLa cell line was cultured in Dulbecco's Modified Eagle Medium (DMEM) (Euroclone, Milan, Italy) supplemented with 10% fetal bovine serum (HyClone™, Cytiva, Marlborough, MA, USA), 2 mM L-glutamine, 100 U/ml penicillin, 100 µg/ml streptomycin (all from Euroclone). $5x10^4$ cells were seeded per each well of a six well. Twenty-four hours post seeding, cells were treated with 2 mM thymidine; after 16 h, cells were washed with DMEM 10% FBS to release after the first block. After further 8 h, cells were treated again with 2 mM thymidine. Sixteen hours after the second block, cells were washed with DMEM 10% FBS and collected each 2 hours for 12 hours. Cells harvested at t = 0 were collected immediately following the DMEM 10% FBS wash. Cells were maintained at 37°C in a humidified atmosphere with 5% CO_2. The cell line was authenticated by short tandem repeat (STR) profiling and routinely screened for mycoplasma contamination.

Transfection of plasmids and siRNAs. Vectors encoding for wild-type or AKAP1 mutants were previously described [17]. ON-TARGET plus siRNA targeting coding regions of human AKAP1 was purchased from Dharmacon (Lafayette, CO, USA). The siRNA sequence (Thermo Scientific) targeting human AKAP1 is the following: GGGAGCAUGUCUUGGAAUU. Control siRNA was purchased from Ambion (am4637). siRNAs were transiently transfected using lipofectamine 2000 (Invitrogen, Carlsbad, California, USA) at a final concentration of 100 pmol/ml of culture medium.

Antibodies and chemicals. A polyclonal antibody directed against murine AKAP1 was raised as described before [13]. Primary antibodies against the following epitopes were used: anti-V5 antibody (1:2000 for immunoblotting; 1:200 for immunoprecipitation, 1:200 for immunostaining, #MCA1360 Bio-Rad, Hercules, CA, USA); GST (1:5,000; #sc-138 Santa Cruz Biotechnology); myc (1:1000 for immunoblotting, 1:200 for immunoprecipitation; #M4439, Merck); DDX6 (1:100 for immunoblotting; 1:100 for immunostaining #SAB4200837, Novus biological); EDC3 (1:1,000 for immunoblotting, #16486 Proteintech); Ago2 (1:1000 for immunoblotting, #ab186733, Abcam); Dicer (1:1,000 for immunoblotting, #20567, Proteintech); CDK1 (1:1000 for immunoblotting, #19532, Proteintech); Phospho-CDK Substrate Motif [(K/H)pSP] MultiMab (1:1000 for immunoblotting, #9477, Cell Signalling); Cyclin B (1:1000 for immunoblotting, #4138, Cell Signalling); Cyclin A (1:1000 for immunoblotting, #20808, Cell Signaling); rabbit anti-AKAP1 (1:1000 for immunoblotting, #A-301-379 Bethyl); mouse anti-γ tubulin (γ TUB; 1:1000 for immunoblotting, # T5326 Sigma-Aldrich). Secondary antibodies used: donkey anti-rabbit IgG HRP linked (1:3000 for immunoblotting, #NA934, GE Healthcare); sheep anti-mouse IgG HRP linked (1:3000

for immunoblotting, #NA931, GE Healthcare). Where indicated, RO3306 (CDK1 inhibitor IV, #217699, Calbiochem) was used at 10 μM.

Immunoprecipitation and western blot analysis. Cells were washed twice with phosphate-buffered saline and lysed in Tris-buffered saline buffer-1% w/v Triton-X 100 (150 mM NaCl; 50 mM Tris-HCl, pH 7.5; 1 mM EDTA; 1 mM NaF; 1 mM $Na_4P_2O_7$; 0.4 mM Na_3VO_4). Lysed cells (1.5 mg) were subjected to immunoprecipitation with the indicated antibodies. Whole-cell lysates (50 μg) and immunoprecipitates were resolved on sodium dodecyl sulfate polyacrylamide gel and transferred on nitrocellulose membrane (Bio-Rad, Milan, Italy) for 10 min. Filters were blocked in Tween-20 Phosphate buffer saline (TPBS) (PBS-Sigma, 0,1% Tween 20, pH 7.4) containing 5% non-fat dry milk, for 1 h, at room temperature. Blots were then incubated with primary antibody, overnight. Blots were washed three times with TPBS buffer and then incubated for 1 h with the secondary antibody (peroxidase-coupled anti-rabbit) (GE-Healthcare, Little Chalfont, UK) in TPBS. Reactive signals were revealed by enhanced ECL western blotting analysis system (Euroclone, EMP001005).

RNA immunoprecipitation. For each AKAP1-associated RNA immunoprecipitation (RIP) reaction, 5 μg of anti-V5 antibody were conjugated to 50 μl of Dynabeads M-280 Sheep Anti-Mouse IgG (Cat. 11201D, Thermo Fisher) by rotating at 4°C, for 4 h. Subsequently, 2 mg of protein lysates, extracted from U87MG cells transiently transfected with pcDNA3.1-AKAP1_WT-V5, pcDNA3.1-AKAP1_Δ563-630-V5, pcDNA3.1-AKAP1_Δ709-786-V5, or pcDNA3.1-V5 (negative control), were added to the beads. The reaction mixtures were supplemented with 35 μl of 0.5 M EDTA and RNase inhibitor to a final concentration of 200 U/ml, then brought to a final volume of 1 ml with NT2 buffer (50 mM Tris-HCl, pH 7.4; 150 mM NaCl; 1 mM $MgCl_2$; 0.05% w/v NP-40). A 20 μl aliquot of diluted protein lysate was reserved and stored at −80°C for later RNA extraction as the “input” control. The tubes containing beads and protein lysate were incubated with rotation at 4°C, overnight. Following incubation, beads were washed four times with 1 ml of NT2 buffer. During the final wash, 10% of the immunoprecipitation reaction was reserved and resuspended in Laemmli buffer for subsequent western blot analysis. The remaining 90% of the beads were resuspended in 150 μl NT2 buffer supplemented with 9 μl of 20 mg/ml Proteinase K (Cat. AM2546, Ambion Inc., Austin, TX, USA) and 7.5 μl of 20% w/v SDS to release RNA-protein complexes. This mixture was incubated at 55°C, for 30 min. Afterward, the supernatant was collected, and the beads were washed with 100 μl NT2 buffer. The combined 250 μl sample was purified using the RNA Clean & Concentrator™-5 Kit (Cat. R1015, Zymo, Irvine, CA, USA) according to the manufacturer’s instructions; RNA was eluted in 20 μl. RNA extraction from the “input” samples was performed in parallel under the same conditions. RNA integrity was assessed using the High Sensitivity RNA ScreenTape kit and 4200 TapeStation system (both Agilent Technologies, Santa Clara, CA, USA). RNA concentration was measured with the Qubit™ RNA High Sensitivity Assay Kit on a Qubit™ 2.0 fluorimeter (both Invitrogen, Carlsbad, CA, USA).

RNA sequencing. RNA immunoprecipitation followed by high-throughput sequencing (RIP-Seq) IP and “input” libraries were prepared using the TruSeq Stranded Total RNA Library Prep Gold kit (Cat. 20020599, Illumina, San Diego, CA, USA). An equimolar pool of libraries at a concentration of 1.2 nM was

sequenced on the NovaSeq 6000 platform (Illumina) using 2 × 100 bp paired-end mode. On average, 32 million reads were obtained for each sample (Supplementary Table S1).

Data analysis. RIP-Seq data analysis was conducted as follows: FASTQ files were generated from BCL files using bcl2fastq (Illumina v2.20.0.422), and read quality was assessed with FastQC (v0.11.9)[84]. Adapter trimming was performed using cutadapt (v3.3)[85]. The resulting FASTQ files were aligned to the human genome (hg38) using STAR (v2.7.11b)[86], with GENCODE v37 annotation used as the reference GTF file. FeatureCounts (v2.0.1)[87] was used to generate raw read counts. On average, 25 million reads were mapped for each sample (Supplementary Table S2). Differential expression analysis and count normalization were carried out using DESeq2 (v1.49.1). All sequencing data are available in ArrayExpress database with the following accession numbers: E-MTAB-16473. Heatmaps were generated using Morpheurs (https://software.broadinstitute.org/morpheus), and Venn diagrams were created using Venny v. 2.1 (Oliveros, J.C. (2007–2015) Venny. An interactive tool for comparing lists with Venn's diagrams. https://bioinfogp.cnb.csic.es/tools/venny/index.html).

Quantitative real-time PCR. Total RNA was reverse transcribed into cDNA using the cDNA Synthesis Kit (BIO-65054, Meridian Bioscience, Cincinnati, OH, USA) following the manufacturer's protocol. Quantitative real-time PCR (qPCR) was performed in triplicate using BlasTaq™ 2X qPCR Master Mix (Cat. G891, Applied Biological Materials Inc., Richmond, BC, Canada) on a LightCycler® 480 Instrument II (Roche, Basel, Switzerland). Relative gene expression levels were calculated using the $2^{-\Delta\Delta Ct}$ method. The primer sequences used are listed below:

CDK1	**Forward Primer: GGGTTCCTAGTACTGCAATTCGG**
	Reverse Primer: GGAATCCTGCATAAGCACATCCT
COX6A1	Forward Primer: TGGCGGTAGTTGGTGTGTCC
	Reverse Primer: AGCGCGACGAAGAAGGTGAG
COX8A	Forward Primer: GGAGGGGAAGCTTGGGATCA
	Reverse Primer: GGACAGAACGGACCCCTTCAC
GGH1	Forward Primer: CCACAGATACTGTTGACGTGGC
	Reverse Primer: CGGAGAGGCTCCACTTATGG
GLRX	Forward Primer: ACAGCTCACGGGAGCAAGAAC
	Reverse Primer: TTAGCCGCGTCAGCAGTTCC
LEPR	Forward Primer: TGTTACGGTTCTGGCCATCAAT
	Reverse Primer: TCCAGGAAACAATCACACAACTGC
LIPA	Forward Primer: TGTGGGTCATTCTCAAGGCA
	Reverse Primer: GCTAGTACAGAAGGCGACGG
MGST1	Forward Primer: CGAACAGATGACAGAGTAGAACGTG
	Reverse Primer: GGTCGGGACCACTCAAGGAA
MSMO	Forward Primer: GGGCATGGGTGACCATTCGTT
	Reverse Primer: TGATGCCGAGAACCAGCATAGAA
NDUFA4	Forward Primer: TCATCGGTCAGGCCAAGAAGC
	Reverse Primer: TTGAACAATGCCAGACGCAAGAG
PMP22	Forward Primer: GTGGGCAATGGACACGCAAC
	Reverse Primer: AGGATCATGGTGGCCTGGAC
PPT1	Forward Primer: CTCGATGCCCAGGAGAGAGC
	Reverse Primer: TGCCAGTATTCGGCTTGCAC
SDHB	Forward Primer: CCCAGACAAGGCTGGAGACA
	Reverse Primer: CTTCGGAAGGTCAAAGTAGAGTCA
TXN	Forward Primer: AGCAGCCAAGATGGTGAAGCA
	Reverse Primer: CCACGTGGCTGAGAAGTCAAC

Mass Spectrometry Analysis. Triplicate protein samples were subjected to 12% T SDS-PAGE. Following staining with colloidal Coomassie blue, entire gel lanes were excised into 12 slices, finely minced, and washed with water. Proteins from each slice were individually *in-gel* reduced, S-alkylated with iodoacetamide, and digested with trypsin. The resulting peptide mixtures were analyzed using a nanoLC-ESI-Q-Orbitrap-MS/MS system comprising an UltiMate 3000 RSLC nano HPLC (Thermo Fisher Scientific, USA) coupled to a Q-ExactivePlus mass spectrometer via a Nanoflex ion source (Thermo Fisher Scientific). Peptides were loaded onto an Acclaim PepMap™ RSLC C18 column (150 mm × 75 µm ID, 2 µm particle size, 100 Å pore size) and eluted with a gradient of solvent B (19.92/80/0.08 v/v/v water/acetonitrile/formic acid) in solvent A (99.9/0.1 v/v water/formic acid), at a flow rate of 300 nl/min. The gradient of solvent B started at 3%, increased to 40% over 40 min, ramped up to 80% in 5 min, held at 80% for 4 min, and returned to 3% in 1 min, followed by a 30 min column re-equilibration before the next run. The mass spectrometer operated in data-dependent acquisition mode, performing a full scan (*m/z* range 375–1500, resolution 70,000, AGC target 3,000,000, maximum injection time 50 ms), followed by MS/MS scans of the 10 most intense ions. MS/MS spectra were acquired over an *m/z* range of 200–2000, using a normalized collision energy of 32%, AGC target of 100,000, maximum injection time of 100 ms, and resolution of 17,500. A dynamic exclusion of 30 sec was applied. Each sample was analyzed in duplicate to enhance peptide identification and protein coverage.

Protein Identification via Database Search. Raw MS and MS/MS data from each lane were merged and processed using Proteome Discoverer v. 2.4 (Thermo Fisher Scientific), employing the Mascot search algorithm v. 2.4.2 (Matrix Science, UK) with the following parameters: UniProtKB human protein database (82492 protein sequences, Sep, 2022) including common contaminants; carbamidomethylation of cysteine as a fixed modification; oxidation of methionine, deamidation of asparagine and glutamine, and pyroglutamate formation from glutamine as variable modifications. Peptide and fragment mass tolerances were set to ± 10 ppm and ± 0.02 Da, respectively. Trypsin was specified as the proteolytic enzyme, allowing up to two missed cleavages. Proteins were considered confidently identified if supported by at least two sequenced peptides and a Mascot score ≥ 30. Final peptide assignments were manually verified through spectral inspection. Results were filtered to a 1% false discovery rate (FDR). To generate a high-confidence list of AKAP1 interactors, all proteins identified in the V5 control were subtracted from those found in the corresponding AKAP1 sample. This subtraction eliminated non-specific binders, ensuring that the remaining proteins represented specific AKAP1 interactors. The mass spectrometry-based proteomics data have been deposited in the ProteomeXchange Consortium via the PRIDE repository[88], under dataset identifier PXD070538.

Bioinformatics Analysis. Functional enrichment analysis of AKAP1 interactors, including Gene Ontology, was performed using Metascape (https://metascape.org/) selecting the *Homo sapiens* database. The STRING online tool (https://string-db.org) was used to visualize and integrate the resulting protein interaction networks.

Immunofluorescence assays. Cells were plated on coverglass, fixed with 4% paraformaldehyde for 20 min, permeabilized with 0.3% w/v Triton for 5 min, and aspecific antibodies binding sites were saturated

by adding 3% w/v BSA for 1 h. Cells were incubated with the specific primary antibodies and then with the fluorescent-conjugated secondary antibodies (Invitrogen 1:200), for 30 min. Nuclei were stained with DAPI (Invitrogen 1:500) for 10 min. Staining was visualized using a Zeiss LSM700 confocal microscope.

MitoTracker™ Dye for Mitochondria Labeling (#M7513, Invitrogen) was used to stain mitochondria in living cells. Cells were incubated with MitoTracker dye at 37°C, for 30 min, in a humidified atmosphere with 5% CO_2. and washed 5 times with DMEM. Statistical analysis of the immunofluorescence assay was performed using GraphPad.

Metabolic assays. The real-time oxygen consumption rate (OCR) of HeLa cells was measured at 37°C using a Seahorse XF Analyzer (Seahorse Bioscience, North Billerica, MA, USA). HeLa cells were plated into specific cell culture microplates (Agilent, USA) at the concentration of 3×10^4 cells/well, and cultured for the last 12 h in DMEM, 10% FBS. OCR was measured in XF media (non-buffered DMEM medium, containing 10 mM glucose, 2 mM L-glutamine, and 1 mM sodium pyruvate) under basal conditions and after the sequential addition of 1.5 µM oligomycin, 2 µM FCCP, and rotenone + antimycin (0.5 µM all) (all from Agilent). Indices of mitochondrial respiratory function were calculated from the OCR profile: basal OCR (before the addition of oligomycin), basal OCR, maximal respiration (calculated as the difference between FCCP rate and antimycin + rotenone rate), spare respiratory capacity (calculated as the difference of FCCP-induced OCR and basal OCR), ATP production (calculated as the difference between basal OCR and oligomycin-induced OCR). Reported data were the mean values ± SEM of four measurements deriving from four independent experiments.

Nascent protein synthesis analysis. Cells were seeded in 10-cm plates. For HPG (Thermo Fisher Scientific) labeling, cells were first incubated in cysteine/methionine-free medium (Sigma-Aldrich) at 37°C, for 30 min, and then 100 µM of HPG was added to the media at 37°C, for 2 h. After harvesting, cells were resuspended in 200 µL of Click-iT lysis buffer (50 mM TRIS-HCl at pH 8, 1% w/v SDS, 250 U/mL Universal Nuclease [Thermo Fisher Scientific]) and incubated on ice for 15 min, followed by sonication with Bioruptor (Diagenode) for 5 cycles, 30 sec ON/OFF, high setting. Cell extracts were centrifuged at 18,000 rcf for 5 min, and protein concentration was determined by BCA assay (Thermo Fisher Scientific). About 80 to 100 µg of proteins were subjected to a click reaction using a commercial kit (Click-iT cell reaction buffer kit; Thermo Fisher Scientific), with 40 µM biotin-azide (Thermo Fisher Scientific). According to the manufacturer's protocol, proteins were purified from the mixture using a MeOH/chloroform approach, after the end of the click reaction. The extracted pellet was dissolved in 20 µL of Click-iT lysis buffer containing 1% w/v SDS, and protein concentration was determined by BCA assay. Equal amounts of proteins were loaded on a 10% Tris-glycine gel and transferred to PVDF membrane. Total protein levels were detected using the no-stain protein labeling reagent (Thermo Fisher Scientific). Upon membrane blocking with 5% v/v milk in T-TBS, nascent protein synthesis was monitored following incubation with streptavidin-HRP using a ChemiDoc MP imaging system (Bio-Rad).

Homology modeling of the WT-AKAP1/RIIβ $_{D/D}$ complex. To construct the complex between the WT amphipathic α-helix of AKAP1 (WT-AKAP1) with the dimerization domain (D/D) of the cAMP-dependent

human protein kinase type II-beta regulatory ($RII\beta_{D/D}$) domain, the homology modeling technique has been adopted. Specifically, the Cryo-EM model of AKAP18-PKA complex (PDB ID: 3J4Q) (**Supplementary Fig. S5 a-b**)[89] was downloaded from the Protein Data Bank (PDB) website (www.rscb.org). In this complex, the human sequence of AKAP18 (*h*AKAP18) binds with its amphipathic α-helix the $RII\alpha_{D/D}$ subunit ok PKA (**Supplementary Fig. S5a**). Thus, the homology modeling was applied in order to: *(i)* build the same sequence of the amphipathic α-helix of AKAP1 used in the experiments (WT-AKAP1); *(ii)* build the $RII\beta_{D/D}$ domain from the $RII\alpha_{D/D}$. The first step has been conducted using as template the mouse sequence of the amphipathic α-helix (UniProtKB code: O08715) and building the homology model with I-Tasser [90] for which only the first model with the highest c-score was used (**Supplementary Fig. S5c**). The second step was carried out by building the homology model of $RII\beta_{D/D}$ from the $RII\alpha_{D/D}$ sequence (identity percentage of 75%) (UniProtKB code: P31323) with the Prime module of Schrödinger (Prime, Schrödinger, LLC, New York, NY, 2022) (**Supplementary Fig. S5d**). From the obtained WT-AKAP1/$RII\beta_{D/D}$ homology model, further mutations were made with the aim to reproduce the experimental conditions. Specifically, from the WT-AKAP1 of the mouse sequence, the double mutation S315A and T322A was made to reproduce the double alanine mutated amphipathic α-helix (namely as *"A2-AKAP1/$RII\beta_{D/D}$"*) (**Supplementary Fig. S8b**). Similarly, the S^{315} and T^{322} were converted into their respective phosphorylated residues, SEP^{315} and TPO^{322} respectively, thus naming the complex as *"P2ST-AKAP1/$RII\beta_{D/D}$"* (**Supplementary Fig. S8c**).

Molecular Dynamics simulations. One μs of conventional Molecular Dynamics simulations (cMDs) of the obtained WT-AKAP1/$RII\beta_{D/D}$, A2-AKAP1/$RII\beta_{D/D}$ and P2ST-AKAP1/$RII\beta_{D/D}$ homology models were carried out with the CUDA version of NAMD ver. 2.13[91]. In addition, the amphipathic α-helix of WT-AKAP1, P2ST-AKAP1 and S315D/T322D (D2ST-AKAP1) system were submitted to three independent cMDs replicas of 500 ns each. Each system was parameterized with the *ff14SB* AMBER force field and immersed in a 16 Å layer cubic water box using the TIP3P water model parameters and then neutralized by adding Na^+ and Cl^- ions. Phosphoserine and Phosphothreonine (SPO and TPO, respectively) were parameterized with the *phosaa10* AMBER force field[92]. A cut-off of 8 Å was used for non-bonded short-range interactions, while long-range electrostatic interactions were computed by means of the Particle Mesh Ewald (PME) method using a 1.0 Å grid spacing in periodic boundary conditions. The SHAKE algorithm was applied to constrain bonds involving hydrogen atoms, with a 2-fs integration time step. Each system was firstly minimized in 4 steps using the conjugate gradient convergence criterion to 0.01 kcal/mol $Å^2$: *(i)* 5000 minimization steps of only hydrogen atoms; *(ii)* 50000 minimization steps of hydrogen atoms and water molecules, keeping the protein restrained with force constant of 50 kcal/mol$Å^2$; *(iii)* 80000 minimization steps of waters and protein side chains, while the protein backbone was restrained with a force constant of 50 kcal/mol$Å^2$; *(iv)* 100000 steps of full minimization, without any constraint. Successively, water molecules, ions and protein atoms were thermally equilibrated in two steps as follows: *(i)* 5 ns of thermal equilibration in NVT ensemble heating with the Langevin thermostat from 0 to 300 K every 50 K by gradually rescaling solute restraints from a force constant from 5 kcal/mol$Å^2$ to zero; *(ii)* 5 ns in NPT

ensemble using the Nosé-Hoover Langevin method at a constant pressure of 1 atm. Finally, the cMD production run was performed in NPT ensemble. Trajectories and data were visualized and analyzed with Visual Molecular Dynamics (VMD) graphics ver. 1.9.3 [93]. All the images were rendered using UCSF Chimera[94].

Well-Tempered Funnel Metadynamics simulation (FM). Following the conventional Molecular Dynamics (cMDs) protocol, the WT-AKAP1/RIIβ$_{D/D}$ system was submitted to Well-Tempered Funnel Metadynamics (FM) simulation[95] using NAMD ver. 2.13 patched with the PLUMED plugin ver. 2.5.3[96]. With this approach, a funnel-shaped restraint (Fig. 5e and **Supplementary Fig. S9 c-d**), in conjunction with Well-Tempered Metadynamics[97], was used to enhance the sampling of the WT-AKAP1 amphipathic α-helix from the RIIβ$_{D/D}$ domain, through multiple recrossing events between the bound and unbound states (**Supplementary Fig. S9a**). All the funnel restraint parameters were set up and visualized utilizing the Funnel-Metadynamics Advanced Protocol (FMAP-GUI) plugin,[98] as follows: a default cylinder radius of 0.1 nm, an α-angle of 0.40 radians for the cone section with a switching point between the cone and the cylinder (Z_{cc}) at 4.0 nm (Fig. 5e). To prevent the amphipathic α-helix of WT-AKAP1 from diffusing into the bulk solvent, a harmonic upper wall was positioned at the end of the cylinder at 6.1 nm from the funnel anchor point, with a kappa value of 10000. The distance collective variable (dist$_{CV}$) between the center of mass (COM) position of the amphipathic α-helix of WT-AKAP1 and the COM of the RIIβ$_{D/D}$ domain (**Supplementary Fig. S10a**) was selected to drive the metadynamics bias (**Supplementary Fig. S11a**). Furthermore, the contactmap (cmap$_{CV}$) and the torsion of the amphipathic α-helix (tors$_{cv}$) collective variables (**Supplementary Fig. S10 b-c, respectively)** were monitored during the FM simulation and used to reconstruct the reweighted free energy surface (FES) (Fig. 5f and Supplementary Fig. S7). The Gaussian deposition rate was every 1000 steps (2 ps) with hills height of 3.0 kJ/mol and a sigma value of dist$_{CV}$ equal to 0.06, while the biasfactor was set to 20. Output of PLUMED files and FM frames were saved every 1000 steps (2 ps). The FM convergence was ensured looking at the decrease of hills height (**Supplementary Fig. S9b**) and the free energy difference between the bound and unbound state (**Supplementary Fig. S11b**).

In vitro kinase assay. CDK2-Cyclin A complexes were purified as described in [99]. Briefly, Cdk2 and Cyclin A were expressed in insect cells using baculovirus, with Cdk2 unmodified and cyclin A carrying an N-terminal 6-His tag (provided by D. O. Morgan, University of California, San Francisco). Proteins were extracted using a Dounce homogenizer in a sodium phosphate buffer with NaCl, glycerol, and protease inhibitors. The cyclin A/CDK2 complex was assembled and activated in vitro with $MgCl_2$, ATP, and phosphatase inhibitors during a 45-minute incubation with cyclin H/CDK7-containing extracts. The complex was purified via Ni-NTA affinity chromatography, anion-exchange chromatography, and Superdex 200 size-exclusion chromatography. Fast-performance liquid chromatography (FPLC) on a Superdex 200 column was performed at 1 ml/min in Tris-HCl/NaCl buffer, with 0.5-ml fractions collected. In parallel, the coding sequence of the AKAP1 was inserted as *Eco*RI/*Xho*I fragment in the plasmid pET42a (Novagen) as GST fusion. *E. coli* BL21 cells were transformed and expression of GST-AKAP1

variants was induced with 0.5 mM IPTG at 37°C for 3 h. Cell pellets were homogenized in PBS-0.5%Triton using a sonicator and clarified lysates were subjected to affinity purification using Glutathione Sepharose Beads (Cytiva, 17-0756-01).

For the in vitro kinase assay 0.5µl of the CDK2-CycA active complex were mixed with 10 µl of the GST-AKAP proteins and suspended in kinase assay buffer (5 mM $MgCl_2$, 2 mM $MnCl_2$, 150 mM NaCl, 20 mM HEPES/KOH pH 7.5, 0.05% NP-40, 0.25 mM DTT) supplemented with phosphatase and protease inhibitor cocktail. Labeled γ-^{32}P ATP (Perkin Elmer) was added to the reaction and incubated at 30°C for 1 h. Samples were denatured with SDS-Laemmli buffer and separated on a SDS-PAGE. Gel was dried and detected with a Phosphoimager device (Amersham). Cdk2 presence was assesed by western-blot using Cdk2 antibodies (SantaCruz, sc-6248).

Mitochondrial analysis. Image processing and analysis were performed in FIJI/ImageJ using a custom macro [100]. Multi-channel microscopy files (e.g., .czi) were imported using the Bio-Formats Importer [101] .For the mitochondria, images were background-corrected using Subtract Background and denoised using a Gaussian blur. Mitochondrial structures then were segmented using auto-thresholding, skeletonized and analyzed with the Analyze Skeleton (2D/3D) plugin to extract network metrics (e.g., branch length)[102] .

Declarations

Conflict of interest.

The authors declare no conflict of interest.

Acknowledgements.

This work was supported by Fondazione AIRC per la Ricerca sul Cancro (IG2023-29124), the Italian Ministry of University and Research (National Center for Gene Therapy and Drugs based on RNA Technology, PNRR-CN3: E63C22000940007; PRIN2022: E53D23009690006 and E53D23021760001), European Regional Development Fund (POR Campania FESR 2021–2027)- grant “RARE.Glials”.

References

1. Lahtvee, P.-J., Kumar, R., Hallström, B. M. & Nielsen, J. Adaptation to different types of stress converge on mitochondrial metabolism. *Mol. Biol. Cell* **27**, 2505–2514 (2016).
2. Rinaldi, L., Senatore, E., Iannucci, R., Chiuso, F. & Feliciello, A. Control of Mitochondrial Activity by the Ubiquitin Code in Health and Cancer. *Cells* **12**, 234 (2023).

3. Cribbs, J. T. & Strack, S. Reversible phosphorylation of Drp1 by cyclic AMP-dependent protein kinase and calcineurin regulates mitochondrial fission and cell death. *EMBO Rep.* **8**, 939–944 (2007).
4. Signorile, A. *et al.* cAMP/PKA Signaling Modulates Mitochondrial Supercomplex Organization. *Int. J. Mol. Sci.* **23**, 9655 (2022).
5. Rinaldi, L., Delle Donne, R., Borzacchiello, D., Insabato, L. & Feliciello, A. The role of compartmentalized signaling pathways in the control of mitochondrial activities in cancer cells. *Biochim. Biophys. Acta Rev. Cancer* **1869**, 293–302 (2018).
6. Carr, D. W., Stofko-Hahn, R. E., Fraser, I. D., Cone, R. D. & Scott, J. D. Localization of the cAMP-dependent protein kinase to the postsynaptic densities by A-kinase anchoring proteins. Characterization of AKAP 79. *J. Biol. Chem.* **267**, 16816–16823 (1992).
7. Feliciello, A., Li, Y., Avvedimento, E. V., Gottesman, M. E. & Rubin, C. S. A-kinase anchor protein 75 increases the rate and magnitude of cAMP signaling to the nucleus. *Curr. Biol. CB* **7**, 1011–1014 (1997).
8. Livigni, A. *et al.* Mitochondrial AKAP121 links cAMP and src signaling to oxidative metabolism. *Mol. Biol. Cell* **17**, 263–271 (2006).
9. Xiang, H. *et al.* AKAP1 Regulates Mitochondrial Dynamics during the Fatty-Acid-Promoted Maturation of Human-Induced Pluripotent Stem Cell-Derived Cardiomyocytes as Indicated by Proteomics Sequencing. *Int. J. Mol. Sci.* **24**, 8112 (2023).
10. Carlucci, A., Lignitto, L. & Feliciello, A. Control of mitochondria dynamics and oxidative metabolism by cAMP, AKAPs and the proteasome. *Trends Cell Biol.* **18**, 604–613 (2008).
11. Flippo, K. H. *et al.* AKAP1 Protects from Cerebral Ischemic Stroke by Inhibiting Drp1-Dependent Mitochondrial Fission. *J. Neurosci. Off. J. Soc. Neurosci.* **38**, 8233–8242 (2018).
12. Trendelenburg, G., Hummel, M., Riecken, E. O. & Hanski, C. Molecular characterization of AKAP149, a novel A kinase anchor protein with a KH domain. *Biochem. Biophys. Res. Commun.* **225**, 313–319 (1996).
13. Carlucci, A. *et al.* Proteolysis of AKAP121 regulates mitochondrial activity during cellular hypoxia and brain ischaemia. *EMBO J.* **27**, 1073–1084 (2008).
14. Cardone, L. *et al.* Mitochondrial AKAP121 binds and targets protein tyrosine phosphatase D1, a novel positive regulator of src signaling. *Mol. Cell. Biol.* **24**, 4613–4626 (2004).
15. Asirvatham, A. L. *et al.* A-kinase anchoring proteins interact with phosphodiesterases in T lymphocyte cell lines. *J. Immunol. Baltim. Md 1950* **173**, 4806–4814 (2004).
16. Furusawa, M., Ohnishi, T., Taira, T., Iguchi-Ariga, S. M. & Ariga, H. AMY-1, a c-Myc-binding protein, is localized in the mitochondria of sperm by association with S-AKAP84, an anchor protein of cAMP-dependent protein kinase. *J. Biol. Chem.* **276**, 36647–36651 (2001).
17. Rinaldi, L. *et al.* Mitochondrial AKAP1 supports mTOR pathway and tumor growth. *Cell Death Dis.* **8**, e2842 (2017).

18. Rogne, M. *et al.* The KH-Tudor domain of a-kinase anchoring protein 149 mediates RNA-dependent self-association. *Biochemistry* **45**, 14980–14989 (2006).
19. Dyson, M. T. *et al.* Mitochondrial A-kinase anchoring protein 121 binds type II protein kinase A and enhances steroidogenic acute regulatory protein-mediated steroidogenesis in MA-10 mouse leydig tumor cells. *Biol. Reprod.* **78**, 267–277 (2008).
20. Ginsberg, M. D., Feliciello, A., Jones, J. K., Avvedimento, E. V. & Gottesman, M. E. PKA-dependent binding of mRNA to the mitochondrial AKAP121 protein. *J. Mol. Biol.* **327**, 885–897 (2003).
21. Zhang, Y., Chen, Y., Gucek, M. & Xu, H. The mitochondrial outer membrane protein MDI promotes local protein synthesis and mtDNA replication. *EMBO J.* **35**, 1045–1057 (2016).
22. Gabrovsek, L. *et al.* A-kinase-anchoring protein 1 (dAKAP1)-based signaling complexes coordinate local protein synthesis at the mitochondrial surface. *J. Biol. Chem.* **295**, 10749–10765 (2020).
23. Williams, C. C., Jan, C. H. & Weissman, J. S. Targeting and plasticity of mitochondrial proteins revealed by proximity-specific ribosome profiling. *Science* **346**, 748–751 (2014).
24. Luo, J. *et al.* Proximity-specific ribosome profiling reveals the logic of localized mitochondrial translation. *Cell* **188**, 5589-5604.e17 (2025).
25. Isaac, R. S., McShane, E. & Churchman, L. S. The Multiple Levels of Mitonuclear Coregulation. *Annu. Rev. Genet.* **52**, 511–533 (2018).
26. Richman, T. R. *et al.* Loss of the RNA-binding protein TACO1 causes late-onset mitochondrial dysfunction in mice. *Nat. Commun.* **7**, 11884 (2016).
27. Richter-Dennerlein, R. *et al.* Mitochondrial Protein Synthesis Adapts to Influx of Nuclear-Encoded Protein. *Cell* **167**, 471-483.e10 (2016).
28. Luo, Y., Na, Z. & Slavoff, S. A. P-Bodies: Composition, Properties, and Functions. *Biochemistry* **57**, 2424–2431 (2018).
29. Senatore, E. *et al.* Praja2 controls P-body assembly and translation in glioblastoma by non-proteolytic ubiquitylation of DDX6. *EMBO Rep.* **26**, 2347–2377 (2025).
30. Parker, R. & Sheth, U. P bodies and the control of mRNA translation and degradation. *Mol. Cell* **25**, 635–646 (2007).
31. Ayache, J. *et al.* P-body assembly requires DDX6 repression complexes rather than decay or Ataxin2/2L complexes. *Mol. Biol. Cell* **26**, 2579–2595 (2015).
32. Bearss, J. J. *et al.* EDC3 phosphorylation regulates growth and invasion through controlling P-body formation and dynamics. *EMBO Rep.* **22**, e50835 (2021).
33. Bhat, M. *et al.* Targeting the translation machinery in cancer. *Nat. Rev. Drug Discov.* **14**, 261–278 (2015).
34. Yang, Z. *et al.* GW182 is critical for the stability of GW bodies expressed during the cell cycle and cell proliferation. *J. Cell Sci.* **117**, 5567–5578 (2004).
35. Feliciello, A., Rubin, C. S., Avvedimento, E. V. & Gottesman, M. E. Expression of a kinase anchor protein 121 is regulated by hormones in thyroid and testicular germ cells. *J. Biol. Chem.* **273**,

23361–23366 (1998).

36. Yu, J., Zhang, Y., Zhou, D., Wu, J. & Luo, R. Higher expression of A-kinase anchoring-protein 1 predicts poor prognosis in human hepatocellular carcinoma. *Oncol. Lett.* **16**, 131–136 (2018).
37. Masui, K. & Mischel, P. S. Metabolic and epigenetic reprogramming in the pathogenesis of glioblastoma: Toward the establishment of “metabolism-based pathology”. *Pathol. Int.* **73**, 533–541 (2023).
38. Labunskyy, V. M., Hatfield, D. L. & Gladyshev, V. N. Selenoproteins: molecular pathways and physiological roles. *Physiol. Rev.* **94**, 739–777 (2014).
39. Kellogg, M. K., Miller, S. C., Tikhonova, E. B. & Karamyshev, A. L. SRPassing Co-translational Targeting: The Role of the Signal Recognition Particle in Protein Targeting and mRNA Protection. *Int. J. Mol. Sci.* **22**, 6284 (2021).
40. Arif, A. *et al.* The GAIT translational control system. *Wiley Interdiscip. Rev. RNA* **9**, e1441 (2018).
41. Awuah, W. A. *et al.* Exploring the role of Nrf2 signaling in glioblastoma multiforme. *Discov. Oncol.* **13**, 94 (2022).
42. Zheng, X. *et al.* Selenoprotein P expression in glioblastoma as a regulator of ferroptosis sensitivity: preservation of GPX4 via the cycling-selenium storage. *Sci. Rep.* **14**, 682 (2024).
43. Varlamova, E. G., Goltyaev, M. V. & Turovsky, E. A. The Role of Selenoproteins SELENOM and SELENOT in the Regulation of Apoptosis, ER Stress, and Calcium Homeostasis in the A-172 Human Glioblastoma Cell Line. *Biology* **11**, 811 (2022).
44. Lin, H. *et al.* Understanding the immunosuppressive microenvironment of glioma: mechanistic insights and clinical perspectives. *J. Hematol. Oncol.J Hematol Oncol* **17**, 31 (2024).
45. Cho, K. F. *et al.* Proximity labeling in mammalian cells with TurboID and split-TurboID. *Nat. Protoc.* **15**, 3971–3999 (2020).
46. Chatr-Aryamontri, A. *et al.* The BioGRID interaction database: 2017 update. *Nucleic Acids Res.* **45**, D369–D379 (2017).
47. Del Toro, N. *et al.* The IntAct database: efficient access to fine-grained molecular interaction data. *Nucleic Acids Res.* **50**, D648–D653 (2022).
48. Licata, L. *et al.* MINT, the molecular interaction database: 2012 update. *Nucleic Acids Res.* **40**, D857-861 (2012).
49. Mellacheruvu, D. *et al.* The CRAPome: a contaminant repository for affinity purification-mass spectrometry data. *Nat. Methods* **10**, 730–736 (2013).
50. Gavet, O. & Pines, J. Progressive activation of CyclinB1-Cdk1 coordinates entry to mitosis. *Dev. Cell* **18**, 533–543 (2010).
51. Krek, W. & Nigg, E. A. Differential phosphorylation of vertebrate p34cdc2 kinase at the G1/S and G2/M transitions of the cell cycle: identification of major phosphorylation sites. *EMBO J.* **10**, 305–316 (1991).

52. Suzuki, K. *et al.* Identification of non-Ser/Thr-Pro consensus motifs for Cdk1 and their roles in mitotic regulation of C2H2 zinc finger proteins and Ect2. *Sci. Rep.* **5**, 7929 (2015).
53. Stokes, M. P. *et al.* Profiling of UV-induced ATM/ATR signaling pathways. *Proc. Natl. Acad. Sci. U. S. A.* **104**, 19855–19860 (2007).
54. Sharma, K. *et al.* Ultradeep human phosphoproteome reveals a distinct regulatory nature of Tyr and Ser/Thr-based signaling. *Cell Rep.* **8**, 1583–1594 (2014).
55. Rigbolt, K. T. G. *et al.* System-wide temporal characterization of the proteome and phosphoproteome of human embryonic stem cell differentiation. *Sci. Signal.* **4**, rs3 (2011).
56. Edwards, G. *et al.* Loss of AKAP1 triggers Drp1 dephosphorylation-mediated mitochondrial fission and loss in retinal ganglion cells. *Cell Death Dis.* **11**, 254 (2020).
57. He, L. *et al.* Hepatic AKAP1 deficiency exacerbates diet-induced MASLD by enhancing GPAT1-mediated lysophosphatidic acid synthesis. *Nat. Commun.* **16**, 4286 (2025).
58. Liu, H. *et al.* AKAP1/PKA-mediated GRP75 phosphorylation at mitochondria-associated endoplasmic reticulum membranes protects cancer cells against ferroptosis. *Cell Death Differ.* **32**, 488–505 (2025).
59. Ewald, J. C., Kuehne, A., Zamboni, N. & Skotheim, J. M. The Yeast Cyclin-Dependent Kinase Routes Carbon Fluxes to Fuel Cell Cycle Progression. *Mol. Cell* **62**, 532–545 (2016).
60. Rizk-Rabin, M. *et al.* Link between steroidogenesis, the cell cycle, and PKA in adrenocortical tumor cells. *Mol. Cell. Endocrinol.* **500**, 110636 (2020).
61. Zhu, M. *et al.* The cAMP-PKA signaling initiates mitosis by phosphorylating Bora. *Nat. Commun.* **16**, 7898 (2025).
62. Glotzer, M., Murray, A. W. & Kirschner, M. W. Cyclin is degraded by the ubiquitin pathway. *Nature* **349**, 132–138 (1991).
63. Hershko, A. The ubiquitin system for protein degradation and some of its roles in the control of the cell division cycle. *Cell Death Differ.* **12**, 1191–1197 (2005).
64. Nurse, P. A long twentieth century of the cell cycle and beyond. *Cell* **100**, 71–78 (2000).
65. Bashir, T., Dorrello, N. V., Amador, V., Guardavaccaro, D. & Pagano, M. Control of the SCF(Skp2-Cks1) ubiquitin ligase by the APC/C(Cdh1) ubiquitin ligase. *Nature* **428**, 190–193 (2004).
66. Lin, D. I. *et al.* Phosphorylation-dependent ubiquitination of cyclin D1 by the SCF(FBX4-alphaB crystallin) complex. *Mol. Cell* **24**, 355–366 (2006).
67. Jang, S.-M., Redon, C. E., Thakur, B. L., Bahta, M. K. & Aladjem, M. I. Regulation of cell cycle drivers by Cullin-RING ubiquitin ligases. *Exp. Mol. Med.* **52**, 1637–1651 (2020).
68. Mitra, K., Wunder, C., Roysam, B., Lin, G. & Lippincott-Schwartz, J. A hyperfused mitochondrial state achieved at G1-S regulates cyclin E buildup and entry into S phase. *Proc. Natl. Acad. Sci. U. S. A.* **106**, 11960–11965 (2009).
69. Schieke, S. M., McCoy, J. P. & Finkel, T. Coordination of mitochondrial bioenergetics with G1 phase cell cycle progression. *Cell Cycle Georget. Tex* **7**, 1782–1787 (2008).

70. Safieddine, A. *et al.* Cell-cycle-dependent mRNA localization in P-bodies. *Mol. Cell* **84**, 4191-4208.e7 (2024).
71. Jia, X. *et al.* Protein translation: biological processes and therapeutic strategies for human diseases. *Signal Transduct. Target. Ther.* **9**, 44 (2024).
72. Decker, C. J. & Parker, R. P-bodies and stress granules: possible roles in the control of translation and mRNA degradation. *Cold Spring Harb. Perspect. Biol.* **4**, a012286 (2012).
73. Feliciello, A., Gottesman, M. E. & Avvedimento, E. V. cAMP-PKA signaling to the mitochondria: protein scaffolds, mRNA and phosphatases. *Cell. Signal.* **17**, 279–287 (2005).
74. White-Gilbertson, S., Kurtz, D. T. & Voelkel-Johnson, C. The role of protein synthesis in cell cycling and cancer. *Mol. Oncol.* **3**, 402–408 (2009).
75. An, T., Liu, Y., Gourguechon, S., Wang, C. C. & Li, Z. CDK Phosphorylation of Translation Initiation Factors Couples Protein Translation with Cell-Cycle Transition. *Cell Rep.* **25**, 3204-3214.e5 (2018).
76. Wang, Z. *et al.* Cyclin B1/Cdk1 coordinates mitochondrial respiration for cell-cycle G2/M progression. *Dev. Cell* **29**, 217–232 (2014).
77. Massacci, G., Perfetto, L. & Sacco, F. The Cyclin-dependent kinase 1: more than a cell cycle regulator. *Br. J. Cancer* **129**, 1707–1716 (2023).
78. Wang, Z. *et al.* Cyclin B1/Cdk1 coordinates mitochondrial respiration for cell-cycle G2/M progression. *Dev. Cell* **29**, 217–232 (2014).
79. Taguchi, N., Ishihara, N., Jofuku, A., Oka, T. & Mihara, K. Mitotic phosphorylation of dynamin-related GTPase Drp1 participates in mitochondrial fission. *J. Biol. Chem.* **282**, 11521–11529 (2007).
80. Newhall, K. J. *et al.* Dynamic Anchoring of PKA Is Essential during Oocyte Maturation. *Curr. Biol.* **16**, 321–327 (2006).
81. Mouery, R. D. *et al.* Proteomic analysis reveals a PLK1-dependent G2/M degradation program and a role for AKAP2 in coordinating the mitotic cytoskeleton. *Cell Rep.* **43**, 114510 (2024).
82. Schiattarella, G. G. *et al.* Akap1 Regulates Vascular Function and Endothelial Cells Behavior. *Hypertens. Dallas Tex 1979* **71**, 507–517 (2018).
83. Das Banerjee, T. *et al.* PINK1 regulates mitochondrial trafficking in dendrites of cortical neurons through mitochondrial PKA. *J. Neurochem.* **142**, 545–559 (2017).
84. de Sena Brandine, G. & Smith, A. D. Falco: high-speed FastQC emulation for quality control of sequencing data. *F1000Research* **8**, 1874 (2019).
85. Martin, M. Cutadapt removes adapter sequences from high-throughput sequencing reads. *EMBnet.journal* **17**, 10 (2011).
86. Dobin, A. *et al.* STAR: ultrafast universal RNA-seq aligner. *Bioinformatics* **29**, 15–21 (2013).
87. Liao, Y., Smyth, G. K. & Shi, W. featureCounts: an efficient general purpose program for assigning sequence reads to genomic features. *Bioinformatics* **30**, 923–930 (2014).
88. Perez-Riverol, Y. *et al.* The PRIDE database resources in 2022: a hub for mass spectrometry-based proteomics evidences. *Nucleic Acids Res.* **50**, D543–D552 (2022).

89. Smith, F. D. *et al.* Intrinsic disorder within an AKAP-protein kinase A complex guides local substrate phosphorylation. *eLife* **2**, e01319 (2013).
90. Yang, J. & Zhang, Y. I-TASSER server: new development for protein structure and function predictions. *Nucleic Acids Res.* **43**, W174-181 (2015).
91. Phillips, J. C. *et al.* Scalable molecular dynamics with NAMD. *J. Comput. Chem.* **26**, 1781–1802 (2005).
92. Steinbrecher, T., Latzer, J. & Case, D. A. Revised AMBER parameters for bioorganic phosphates. *J. Chem. Theory Comput.* **8**, 4405–4412 (2012).
93. Humphrey, W., Dalke, A. & Schulten, K. VMD: visual molecular dynamics. *J. Mol. Graph.* **14**, 33–38, 27–28 (1996).
94. Pettersen, E. F. *et al.* UCSF Chimera--a visualization system for exploratory research and analysis. *J. Comput. Chem.* **25**, 1605–1612 (2004).
95. Limongelli, V., Bonomi, M. & Parrinello, M. Funnel metadynamics as accurate binding free-energy method. *Proc. Natl. Acad. Sci. U. S. A.* **110**, 6358–6363 (2013).
96. Tribello, G. A., Bonomi, M., Branduardi, D., Camilloni, C. & Bussi, G. PLUMED 2: New feathers for an old bird. *Comput. Phys. Commun.* **185**, 604–613 (2014).
97. Barducci, A., Bussi, G. & Parrinello, M. Well-tempered metadynamics: a smoothly converging and tunable free-energy method. *Phys. Rev. Lett.* **100**, 020603 (2008).
98. Raniolo, S. & Limongelli, V. Ligand binding free-energy calculations with funnel metadynamics. *Nat. Protoc.* **15**, 2837–2866 (2020).
99. Hengst, L., Göpfert, U., Lashuel, H. A. & Reed, S. I. Complete inhibition of Cdk/cyclin by one molecule of $p21^{Cip1}$. *Genes Dev.* **12**, 3882–3888 (1998).
100. Schindelin, J. *et al.* Fiji: an open-source platform for biological-image analysis. *Nat. Methods* **9**, 676–682 (2012).
101. Linkert, M. *et al.* Metadata matters: access to image data in the real world. *J. Cell Biol.* **189**, 777–782 (2010).
102. Arganda-Carreras, I., Fernández-González, R., Muñoz-Barrutia, A. & Ortiz-De-Solorzano, C. 3D reconstruction of histological sections: Application to mammary gland tissue. *Microsc. Res. Tech.* **73**, 1019–1029 (2010).

Figures

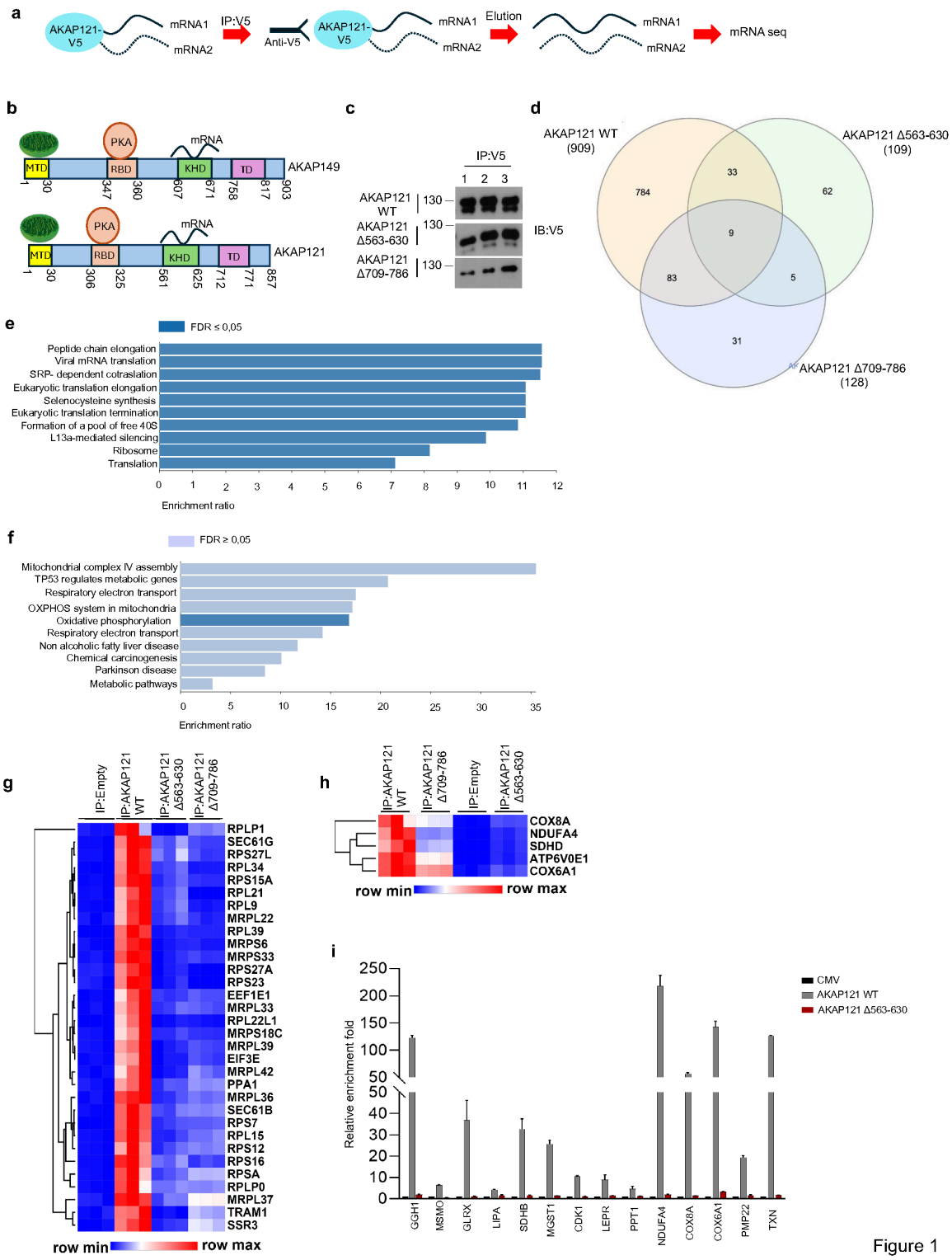


Figure 1

Figure 1

Network analysis of the AKAP1-RNA interactome. (a) Schematic representation of the RNA immunoprecipitation sequencing (RIP-seq) workflow used to identify RNA targets bound by AKAP1. Cells expressing V5-tagged AKAP1 (wild-type (WT) or deletion mutants) were subjected to immunoprecipitation (IP) using an anti-V5 antibody to isolate AKAP1–RNA complexes. Bound RNAs were eluted and analysed by total RNA sequencing (RNA-seq) to determine the transcriptome associated

with each AKAP1 variant. **(b)** Schematic representation of both human AKAP149 and mouse AKAP121 amino acid sequences. **(c)** Immunoblot showing the enrichment of V5-tagged WT AKAP1 and its deletion mutants lacking KH and Tudor domains (Δ563–630 and Δ709–786, respectively) following IP from lysates of U87MG cells transiently transfected with the corresponding constructs. **(d)** Venn diagram illustrating the number of significantly enriched transcripts ($Log_2FC > 2$, padj < 0.01) identified by RIP-Seq for WT AKAP1 and its deletion mutants. Transcripts uniquely bound by WT AKAP1 (orange), as well as those shared between WT and Δ709–786 (violet), were selected for downstream filtering and functional analysis. (**e, f**) Bar plots showing enriched signalling pathways associated with transcripts specifically bound to WT AKAP1 **(e)** or shared between WT and Δ709–786 **(f)**. Dark blue bars indicate statistically significant enrichment (FDR < 0.05), while light blue bars represent non-significant results (FDR > 0.05). Bar height corresponds to the enrichment ratio. **(g)** Hierarchical clustering heatmap displaying normalized expression levels of WT AKAP1-specific transcripts across all RIP-Seq samples. Transcripts included in the heatmap correspond to those involved in the signaling pathways shown in the panel (d). **(h)** Heatmap showing the expression profiles of mRNAs involved in oxidative phosphorylation, enriched in both WT and Δ709–786 RIP datasets. **(i)** Validation of RIP-Seq results by RIP-qPCR. Bar plots show the fold enrichment relative to the empty vector RIP for mRNAs specifically bound to AKAP1 WT and those interacting with both WT and the Δ709–786 AKAP1 mutant. AKAP1 lacking RNA-binding KH domain (Δ563–630) was used as an additional negative control.



Figure 2

Figure 2

Proteomic analysis of AKAP1 interactors by Proximity Ligation Assay. (a) Workflow for proximity labelling assay and proteomic analysis. HeLa cells were transfected with an AKAP1-V5-TurboID construct to enable ATP-dependent biotinylation of proteins within ~10–20 nm of AKAP1. Biotinylated proteins were affinity-purified, resolved by SDS-PAGE, digested, and analyzed by nLC-ESI-Q-Orbitrap-MS/MS. **(b)** Gene Ontology (GO) enrichment analysis of biological processes associated with AKAP1

interactors, performed using Metascape. **(c)** GO enrichment analysis of molecular functions of AKAP1 interactors, performed using Metascape. **(d)** Protein–protein interaction (PPI) network of AKAP1-associated proteins generated using the STRING database (medium confidence score: 0.4). The network includes 59 nodes and 213 edges, with an average node degree of 7.22, average local clustering coefficient of 0.548, and a PPI enrichment p-value < 1.0e-16. **(e)** Clustering of AKAP1 interactors retrieved from the STRING database and analyzed using the K-means algorithm. Members of different functional groups are highlighted in diverse colors.

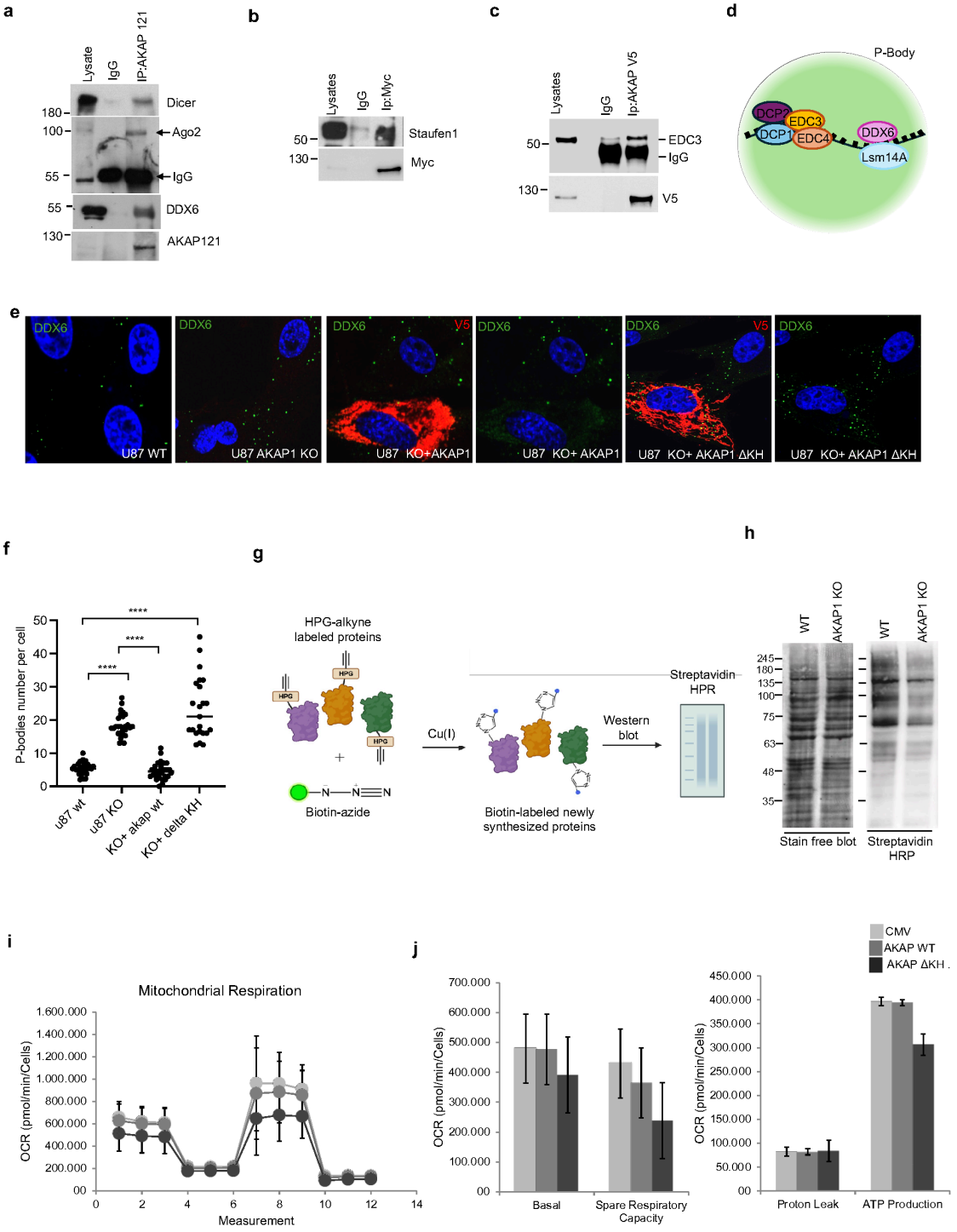


Figure 3

Figure 3

AKAP1 regulates P-bodies dynamics and protein translation. (a) HeLa cells transfected with AKAP1. Cell lysates were immunoprecipitated with anti AKAP1. Lysates and precipitates were immunoblotted with anti-Dicer, anti-DDX6, anti-Ago2 and anti-AKAP1. **(b**) HeLa cells transfected with anti AKAP-Myc were immunoprecipitated with anti Myc. Lysates and precipitates were immunoblotted with anti Staufen and anti-Myc. **(c)** HeLa cells transfected with anti-AKAP1-V5 were immunoprecipitated with anti-V5. Lysates and precipitates were immunoblotted with anti-EDC3 and anti-V5. **(d)** Schematic representation of p-Bodies core components. **(e)**U87MG WT**,** and AKAP1-KO U87MG overexpressing an empty vector, AKAP1-WT and AKAP1-DKH were fixed and immunostained for DDX6, V5 and DAPI. **(f)** Statistical analysis of the experiment in (e). Mean value of three independent experiments ± SEM is indicated. *t* test ****$P < 0.0001$. **(g)** Schematic representation of the nascent protein synthesis assay. **(h)** U87MG WT and AKAP1 KO were grown in cysteine/methionine-free medium at 37 °C, for 30 min, before labeling with 100 µM HPG-alkyne for 2 h. Lysates were subjected to a click reaction with a biotin-azide, loaded on SDS-PAGE, and detected with streptavidin-HRP antibody. **(i)** Kinetic profile of oxygen consumption rate (OCR) in HeLa cells overexpressing empty vector, AKAP1 WT, and AKAP1-DKH. The data are shown as mean ± S.E.M. of three independent experiments, each of them in technical duplicates derived from the same number of seeded cells (3×10^4/well). OCR was measured in real time, under basal conditions, and in response to the indicated mitochondrial inhibitors: oligomycin, FCCP, antimycin A and rotenone.**(j)** Indices of mitochondrial respiratory function, calculated from the OCR profile of HeLa cells: basal respiration, spare respiratory capacity, proton leak and ATP production. Data are expressed as mean ± S.E.M. of three measurements deriving from three independent experiments, each of them in technical duplicates.

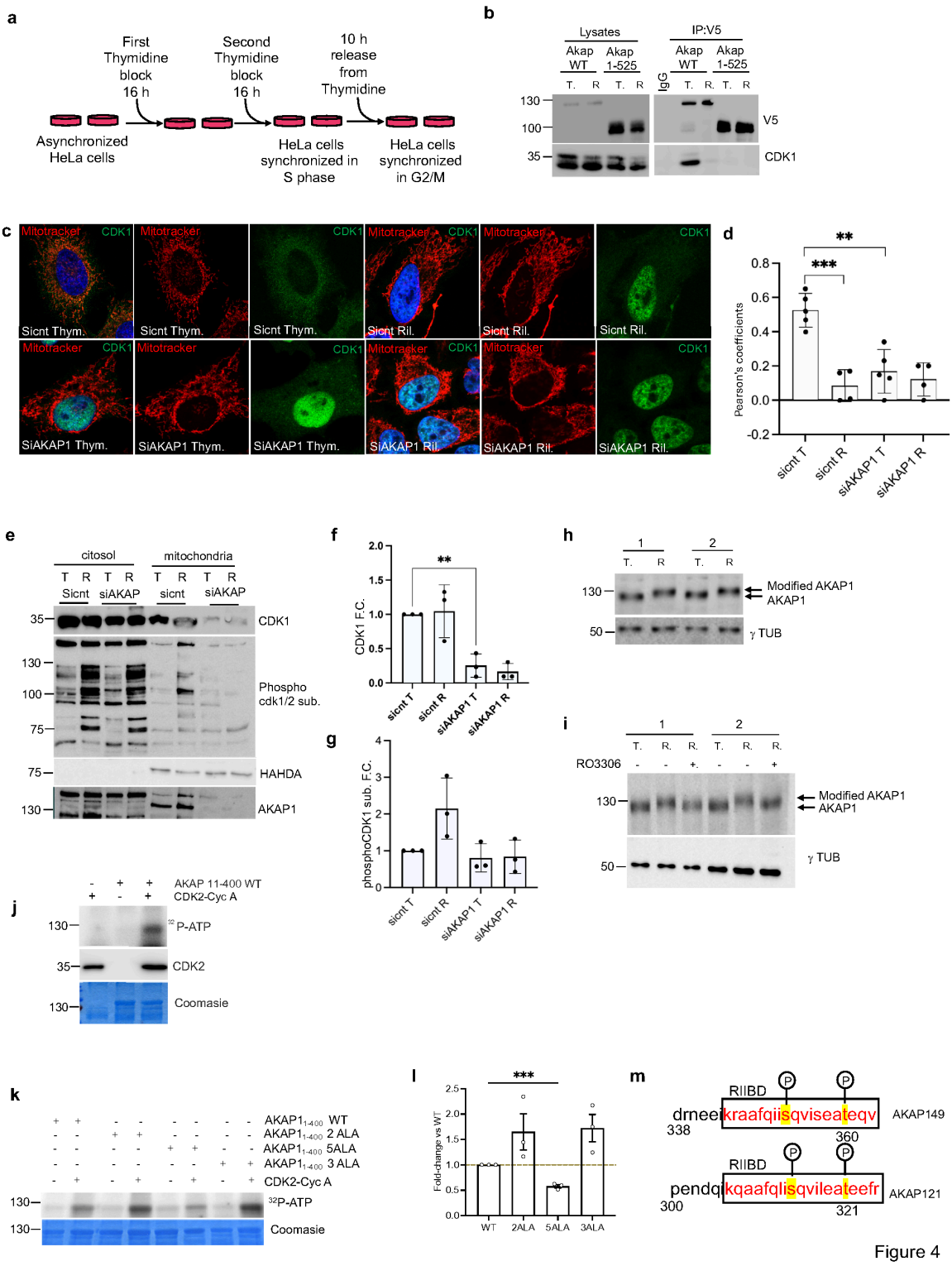


Figure 4

Figure 4

AKAP1 binds and targets mitotic kinases CDK1 to mitochondria. (a) Schematic representation of thymidine synchronization. **(b)** HeLa cells transfected with vectors for AKAP1-V5 WT or AKAP-1-525-V5 were synchronized by thymidine block. Four hours after block, cells were lysed and immunoprecipitated with anti-V5. Lysates and precipitates were immunoblotted with anti-CDK1 and anti-V5. **(c)**HeLa cells AKAP1 transfected with siRNA for AKAP1 or scramble siRNA were synchronized by double thymidine

block. Four hours after release from the block, cells were labeled with mitotracker dye, fixed and immunostained with anti-CDK1 and DAPI. **(d)** Statistical analysis of the experiments shown in (c). Mean value of five independent experiments ± SEM is indicated. *t* test ***$P < 0.001$; **$P < 0.01$. **(e)** Mitochondria and cytosolic fractions from HeLa cells transfected with siRNA for AKAP1 or scramble siRNA and synchronized by double thymidine block. Lysates from both fractions were immunoblotted with anti-CDK1, anti Phospho-CDK1 substrates, anti HA-HDA and anti-AKAP1. **(f)**Statistical analysis of mitochondrial CDK1 (fold changes) shown in (e). Mean value of three independent experiments ± SEM is indicated. *t* test **$P<0.01$. **(g)** Statistical analysis of mitochondrial pCDK1 substrates (fold changes) shown in (e). Mean value of three independent experiments ± SEM is indicated. **(h)** HeLa cells were synchronized by double thymidine block and lysed either immediately (T) or 10 hours after release (R). Samples were loaded in duplicate (1,2) and immunoblotted with anti- AKAP1 and anti- g TUB, as a loading control. **(i)** HeLa cells were synchronized by double thymidine block and lysed either immediately (T) or 10 hours after release in the absence or presence of RO3306 (10 mM; R). Samples were loaded in duplicate in two-fold increasing amounts (1,2) and immunoblotted with anti- AKAP1 and anti- g TUB, as a loading control. **(j)** In vitro kinase assay of the GST-AKAP and the His-tagged CDK2-Cyclin A recombinant proteins. Radiolabeling signal using γ-^{32}P ATP is shown in the upper panel, Western blot detection using CDK2 mouse antibodies (mAb) in the middle, and Coomassie staining of the gel in the lower panel. **(k)** Same assay including the AKAP1 2A (S315A/T322A), 5A (S315A/T322A/S55A/S210A/S449A), and 3A (S315A/T322A/S55A) mutants. Representative gels of N = 3 independent experiments. **(l)** Quantification of the CDK2+ signals normalized against WT Mean ± SEM N=3 Unpaired t test *** p-value≤0.001 **(m)**Schematic representation of the AKAP1 RIIb-binding domain (RIIBD), including the known phosphorylated sites.

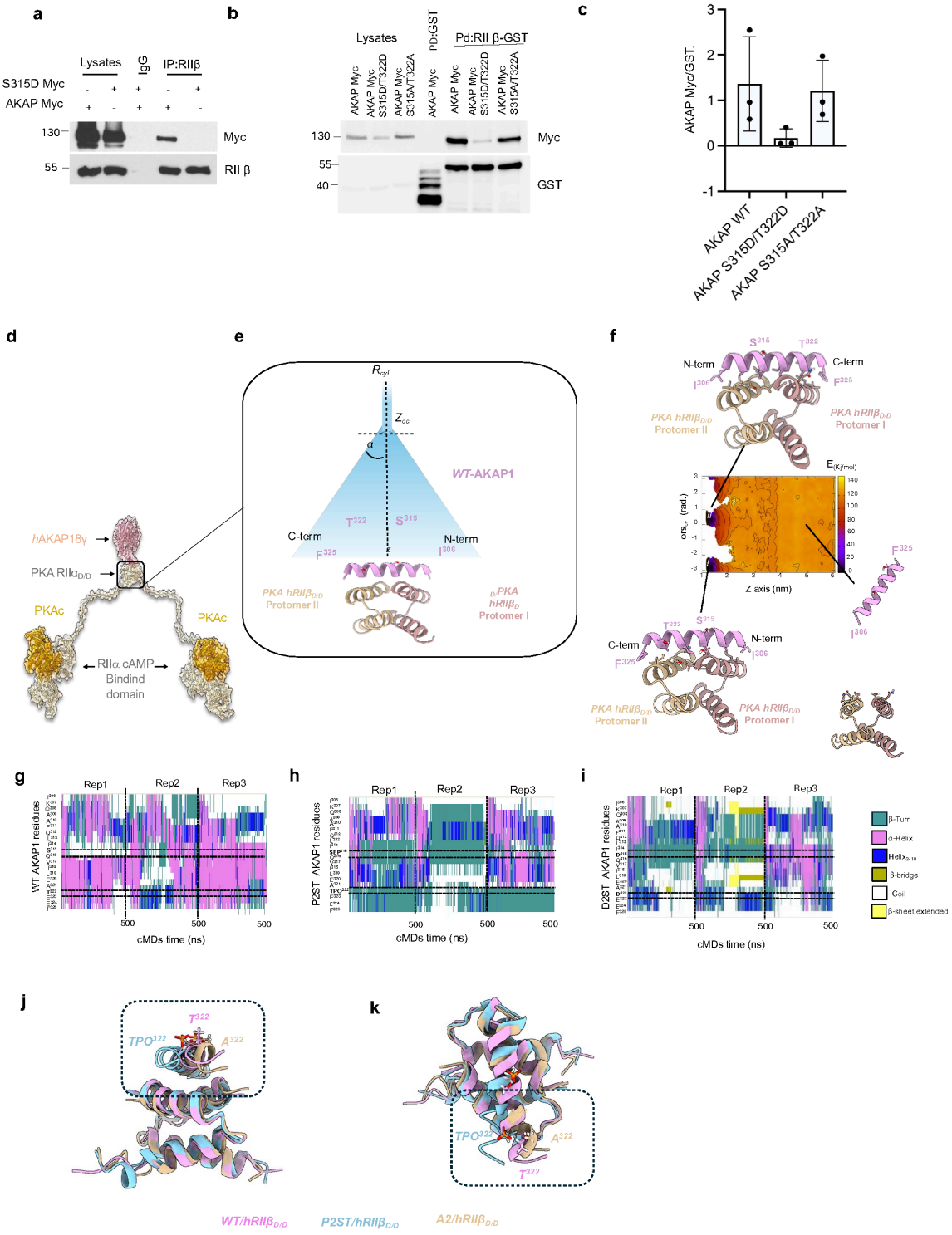


Figure 5

Figure 5

CDK1 phosphorylation of AKAP1 attenuates PKA binding. (a) Lysates from HeLa cells overexpressing AKAP1 WT-Myc or AKAP S315D-Myc were immunoprecipitated with anti-RIIb. Lysates and precipitates were immunoblotted with anti RIIb and anti Myc. **(b)** Lysates from HeLa cells overexpressing AKAP1 WT-Myc, AKAP1-S315A/T322A-Myc and AKAP1-S315D/T322D-Myc were subjected to pull-down assay with purified GST or GST-RIIb. **(c)** Statistical analysis of the experiment in (b). Mean of three independent

experiments ± SEM is indicated. **(d)** Cryo-EM model of AKAP18-PKA complex (PDB ID: 3J4Q) used to build the homology model of WT-AKAP1 amphipathic alpha-helix (plum cartoon) bound to the hRIIβD/D (tan and brown cartoon) **(e)** Last cMDs frame of WT-AKAP1/hRIIβD/D complex with the applied funnel-shaped restraint potential. **(f)** 2D Free Energy Surface (BFES) reweighted as function of funnel Z axis and WT-AKAP1 amphipathic alpha-helix torsion ($Tors_{CV}$) CVs, with the representative energetic minima extracted from basins I and II. **(g-i)** Per-residue secondary structure maps of the amphipathic AKAP1 α-helix in solution, derived from three independent cMD replica trajectories, are shown for the WT protein **(g)**, the T322/S315 double-phosphorylated variant (P2ST-AKAP1) **(h)**, and the T322D/S315D double mutant (D2ST-AKAP1) **(i)**. **(j-k)** Front **(j)** and top **(k)** views of the representative cluster conformations obtained after 1 μs of cMD simulations of the WT, P2ST and A2 AKAP1 variants in complex with the hRIIβ D/D domain. The corresponding complexes are shown as cartoons and coloured light magenta (WT), light cyan (P2ST) and wheat (A2), respectively. Dashed rectangular highlights the different orientation and the loss of the amphipathic α-helix secondary in proximity of phosphorylated T322 (TPO322).

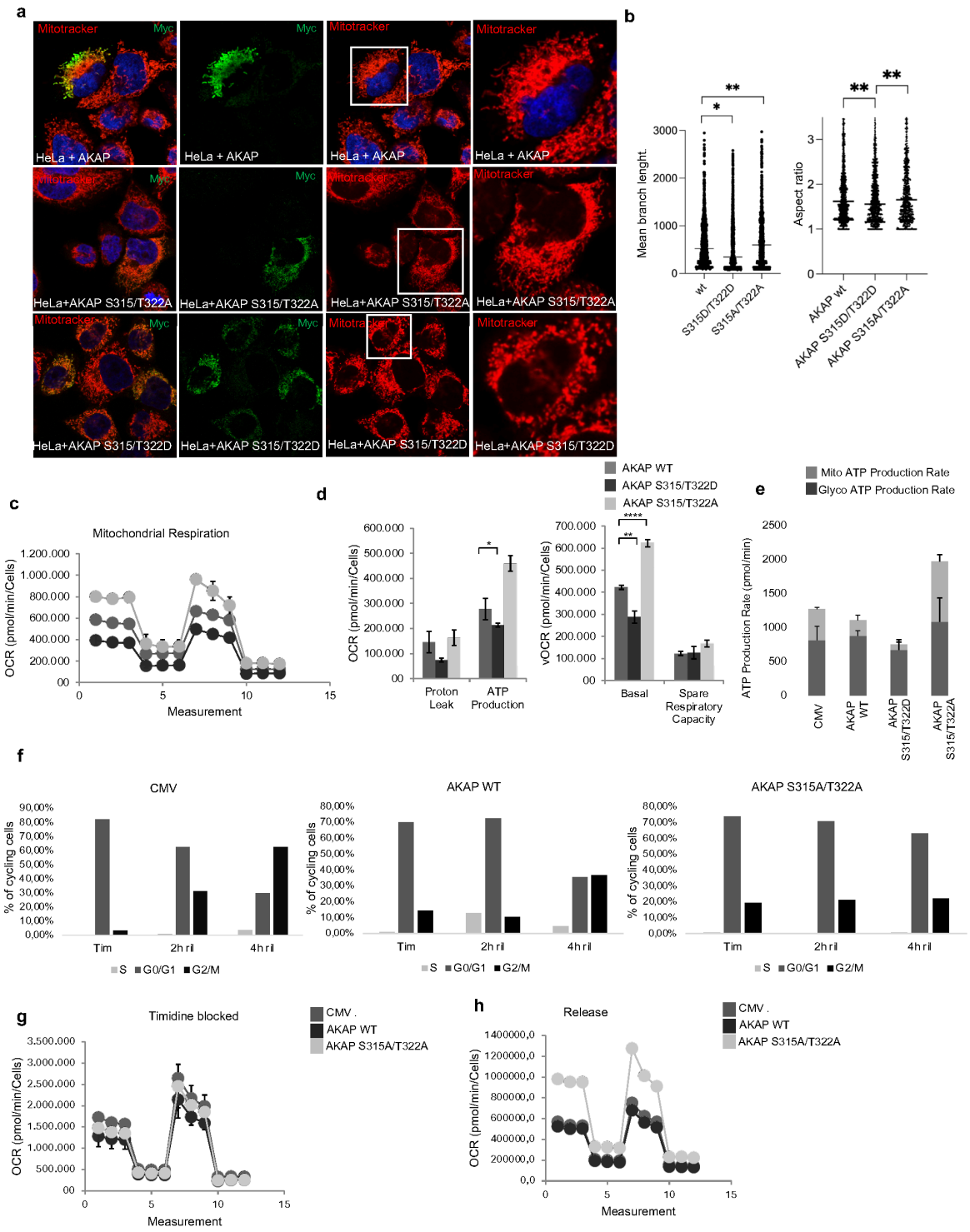


Figure 6

Figure 6

CDK1 phosphorylation of AKAP1 in the RB domain is necessary to regulate cell cycle progression (a) HeLa cells overexpressing AKAP WT-Myc, AKAP S315A/T322A-Myc and AKAP S315D/T322D-Myc were labelled with mitotracker, fixed and immunostained with anti-Myc and DAPI. **(b)** Statistical analysis of the experiments shown in (a). Mean value of three independent experiments ± SEM is indicated. *t* test ***P< 0.001; **P< 0.01; *P< 0.1. **(c)** Kinetic profile of oxygen consumption rate (OCR) in HeLa cells

overexpressing AKAP1 WT, AKAP1-S315A/T322A and AKAP1-S315D/T322D. The data are shown as mean ± S.E.M. of three independent experiments, each of them in technical duplicates derived from the same number of seeded cells (3×10^4/well). OCR was measured in real time, under basal conditions, and in response to the indicated mitochondrial inhibitors: oligomycin, FCCP, antimycin A and rotenone. **(d)** Indices of mitochondrial respiratory function, calculated from the OCR profile of HeLa cells: basal respiration, spare respiratory capacity, proton leak and ATP production. Data are expressed as mean ± S.E.M. of three measurements deriving from three independent experiments, each of them in technical duplicates. **(e)** ATP production rates from mitochondrial respiration (mitoATP) and glycolysis (glycoATP) of HeLa cells overexpressing empty vector (CMV), AKAP 121 WT, AKAP1 S315A/T322A and AKAP S315D/T322D were measured at real-time status following a sequential injection of oligomycin (1.5 μM) and rotenone (0.5 μM). Data are expressed as mean ± S.E.M. of three measurements deriving from three independent experiments, each of them in technical duplicates. **(f)** FACS analysis of HeLa cells stably transfected with empty vector (CMV), AKAP1 WT and AKAP1 S315A/T322A, synchronized by double thymidine block and released after 2 and 4 h from the block. Cell cycle distribution (G0/G1, S, and G2/M) is indicated as percentage of total cells scored. **(g)** Kinetic profile of OCR in HeLa cells stably transfected with empty vector (CMV), AKAP1 WT and AKAP1 S315A/T322A, synchronized by double thymidine block. The data are shown as mean ± S.E.M. of three independent experiments, each of them in technical duplicates derived from the same number of seeded cells (3×10^4/well). OCR was measured in real time, under basal conditions, and in response to the indicated mitochondrial inhibitors: oligomycin, FCCP, antimycin A and rotenone. **(h)** Kinetic profile of OCR in HeLa cells stably transfected with empty vector (CMV), AKAP1 WT and AKAP1 S315A/T322A, released after thymidine block. The data are shown as mean value ±S.E.M. of three independent experiments, each of them in technical duplicates derived from the same number of seeded cells (3×10^4/well). OCR was measured in real time, under basal conditions, and in response to the indicated mitochondrial inhibitors: oligomycin, FCCP, antimycin A and rotenone. Panel g and h share the same colour legend (shown on the right).

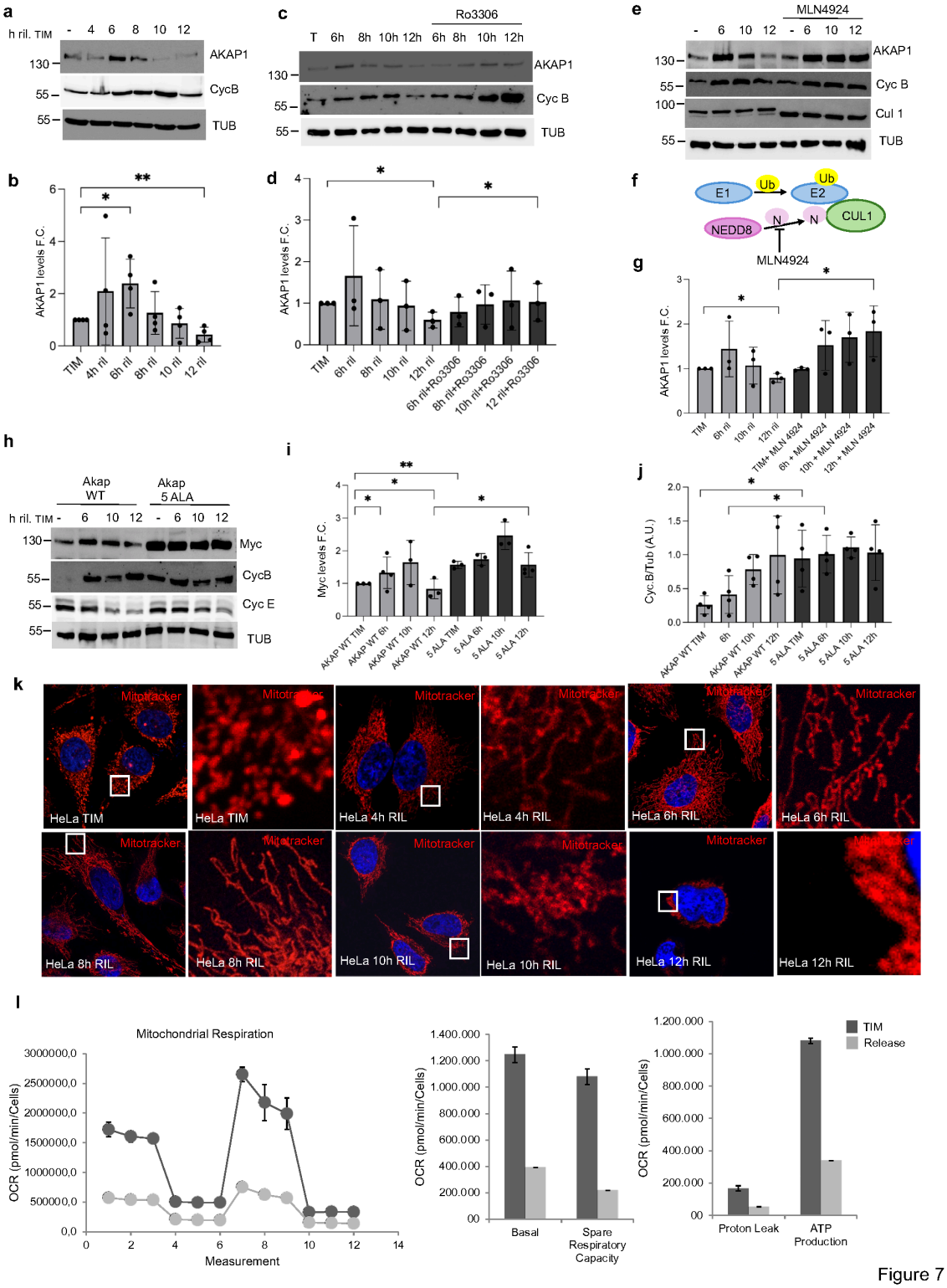


Figure 7

Figure 7

Proteolysis of AKAP1 at mitosis reshapes mitochondrial morphology and activity. (a) Lysates from HeLa cells synchronized by double thymidine (TIM) block and released from the block for the indicated time points were lysed and immunoblotted with anti-AKAP1 and anti-cyclin B. Anti-tubulin was used ad loading control. **(b)** Statistical analysis of the experiment shown in (a). Mean value of four independent experiments ± SEM is indicated. *t* test **P*< 0.05; ***P*<0.01. **(c)** Lysates from HeLa cells synchronized by

double thymidine block. Cells were treated with Ro3306 (10 mM) and released from the block for the indicated time points. Lysates were immunoblotted with anti-AKAP1 and anti-cyclin B. Anti-tubulin was used ad loading control. **(d)** Statistical analysis of the esperiments shown in (c). Mean value of three independent experiments ± SEM is indicated. *t* test **P* < 0.05. **(e)** Lysates from HeLa cells synchronized by double thymidine block. Cells were treated with MLN4924 (10 mM) and then released from the block for the indicated time points. Lysates were immunoblotted with anti-AKAP1, anti-cyclin B and anti-Cul1. Anti-tubulin antibody was used as loading control. **(f)** Schematic picture showing MLN4924 inhibition of CUL1. MLN4924 inhibits the Neddilation of Cullin1, which is necessary to activate the E3 ligase activity of the enzyme. **(g)** Statistical analysis of the esperiment in (e). Mean value of three independent experiments ± SEM is indicated. *t* test **P* < 0.05. **(h)** Lysates from HeLa cells overexpressing AKAP1-WT-Myc or AKAP1-5ALA-Myc and synchronized by double thymidine block. Cells released from the block for the indicated time points were lysed and immunoblotted with anti-Myc, anti-cyclin B and anti-cyclin E. Anti-tubulin was used as loading control. **(i)** Statistical analysis of the experiments shown in (h). Mean value (fold changes) of myc from three independent experiments ± SEM is indicated. *t* test **P* < 0.05; ***P*<0.01. **(j)** Statistical analysis of the experiments shown in (h). Mean value of cyclin B/tubulin from three independent experiments ± SEM is indicated. *t* test **P* < 0.05. **(k)** HeLa cells synchronized by double thymidine (TIM) block and released from the block for the indicated time points were labelled with mitotracker, fixed and stained with DAPI. **(l)** Kinetic profile of OCR in HeLa cells synchronized by double thymidine block and released for 4 h. The data are shown as mean value ± S.E.M. of three independent experiments, each of them in technical duplicates derived from the same number of seeded cells (3×10^4/well). OCR was measured in real time, under basal conditions, and in response to the indicated mitochondrial inhibitors: oligomycin, FCCP, antimycin A and rotenone. All figures shown in panel l share the same colour legend (shown on the right).

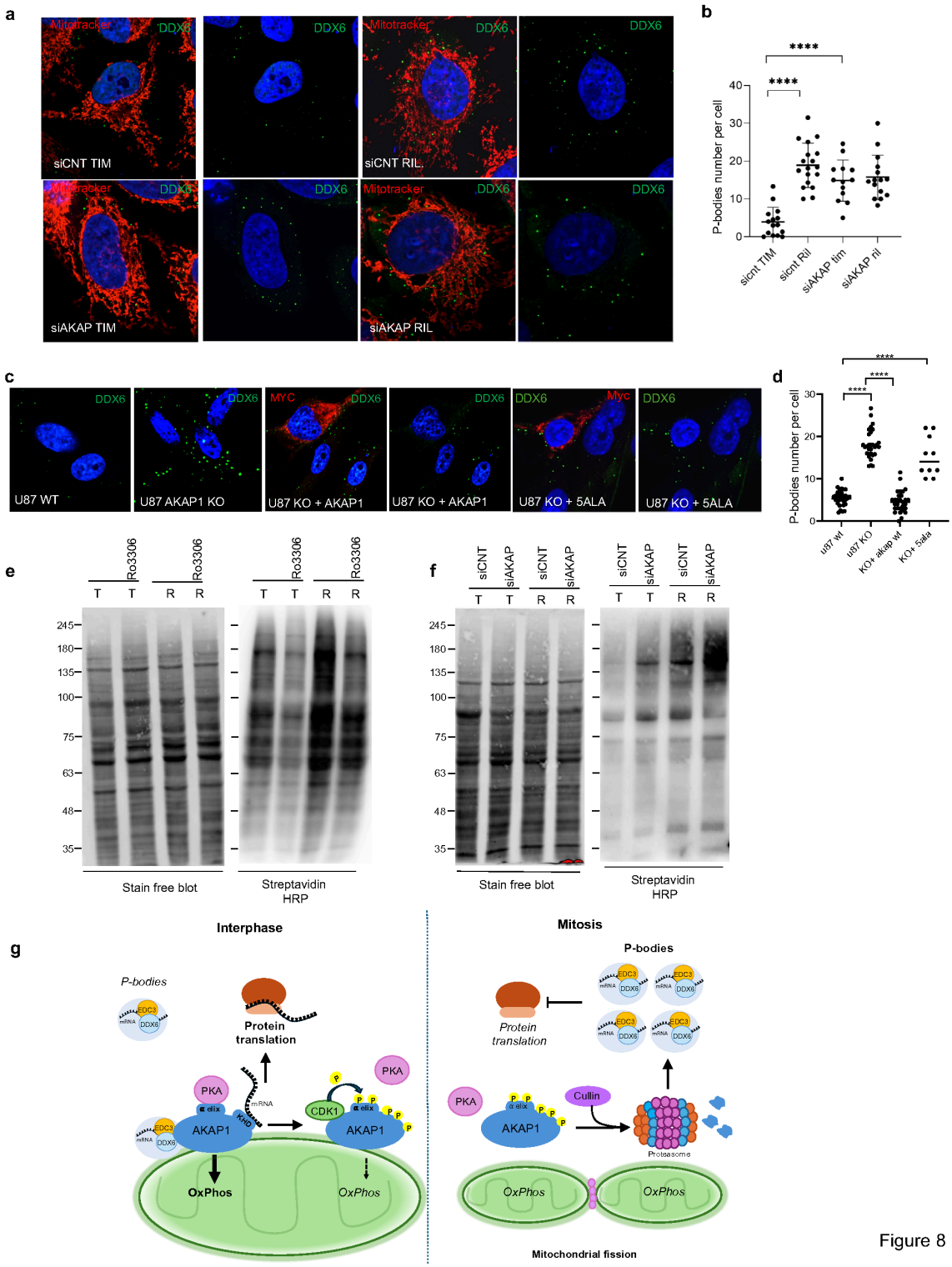


Figure 8

Figure 8

Control of P-body dynamics and protein translation by AKAP1. (a) HeLa cells transfected for AKAP1 and then treated with siRNA for AKAP1 or scramble siRNA were synchronized by double thymidine block, released from the block for 4 h and labeled with mitotracker dye. Cells then were fixed and immunostained with anti-DDX6 and DAPI. **(b)** Statistical analysis of the experiments shown in (a). Mean value of five independent experiments ± SEM is indicated. *t* test ****$P < 0.0001$. **(c)**U87MG WT and

AKAP1-KO U87MG transfected cells with an empty vector or with vectors encoding for AKAP1 WT and AKAP1-5ALA were fixed and immunostained for DDX6, MYC and DAPI. **(d)** Statistical analysis of the experiments shown in (c). Mean value of three independent experiments ± SEM is indicated. *t* test ****$P < 0.0001$. **(e)** HeLa cells synchronized by double thymidine block were treated with Ro3306 (10 mM) and then released for 4 h. Cells were grown in cysteine/methionine-free medium for 30 min at 37 °C before labeling with 100 µM HPG-alkyne for 2 h. Resulting lysates were subjected to a click reaction with biotin-azide, loaded on SDS-PAGE, and detected with streptavidin-HRP antibody. **(f)** HeLa cells AKAP1 transfected with siRNA for AKAP1 or scramble siRNA were synchronized by double thymidine block. Cells were grown in cysteine/methionine-free medium for 30 min at 37 °C before labeling with 100 µM HPG-alkyne for 2 h. Resulting lysates were subjected to a click reaction with biotin-azide, loaded on SDS-PAGE, and detected with streptavidin-HRP antibody. **(g)** Schematic model of the role of AKAP1 in coordinating cell cycle progression, mitochondrial metabolism and protein synthesis regulation. In interphase AKAP1 binds to PKA, favoring the oxidative phosphorylation within the mitochondrial compartment. AKAP1 also binds to mRNAs, DDX6 and EDC3, core components of P-bodies, favoring the protein translation. As the cell approaches to the M phase, CDK1 phosphorylates AKAP, causing the detachment of PKA from the mitochondria and the decrease of the oxidative phosphorylation. In Mitosis, the increased AKAP1 phosphorylation enhances its proteasomal degradation, causing mitochondrial fission and the decrease of specific mRNAs translation.

Supplementary Files

This is a list of supplementary files associated with this preprint. Click to download.

- supplementarytableS1.xlsx
- supplementarytables2.xlsx
- suppl.pdf